博士学位論文

Numerical Investigation of Unsteady External Flows by Cartesian Cut-Cell Method

2020年9月

岩手大学大学院　工学研究科
竹田　裕貴

Numerical Investigation of Unsteady External Flows by Cartesian Cut-Cell Method

Yuki Takeda

Abstract

Unsteady external flow simulation is a major topic of the numerical simulations, and compressibility is significant on the flows in the aerospace engineering. A Cartesian grid solver for unsteady flow simulations receives considerable attention with the improvement of the supercomputing performance and simulation scheme. Cartesian grid has advantages to the boundary fit grid such as the easiness to improve the spatial accuracy of the simulation and the robustness of the mesh generation. In the high-speed flow dynamics, Reynolds number based on the length of the object increases. Unsteady numerical simulation of the high Reynolds number flow has a difficulty of the grid resolution of the turbulence boundary layer and it more significant in the Cartesian grid solver.

Present study investigates computational fluid dynamics (CFD) result of unsteady external flows by Cartesian cut-cell method so that to improve the numerical prediction method for the high Reynolds number flow. Cartesian cut-cell method is one of the most accurate Cartesian grid solvers. The present study contains five chapters. Chapter 1 is the introduction of the present study. Chapter 2 to chapter 4 are shows the result and discussions of the unsteady CFD results. Chapter 2 shows the validation of the inviscid CDF analysis for the flow includes "sharp-edge separations" using Cartesian cut-cell method. Chapter 3 shows the CFD result and discussions for the wall-modeled Cartesian cut-cell method. Chapter 4 shows the coupled CFD analysis and the aerodynamic force modeling of the unsteady flow with pitching motion of reentry capsule. Chapter 5 is the conclusion of the present study.

In chapter 2, the CFD analysis of inviscid compressible flow using the Cartesian cut-cell method are performed. Numerical simulations of the flow past a triangular column are performed as a validation problem of the applicability of the inviscid simulation to the flow around a body with sharp-edge separation. In two-dimensional simulations, the difference between the calculated and experimental values of the drag coefficient, contrary to expectations, increase as the grid width is refined. In these simulations, it is found that vortex shedding is accompanied by a markedly accelerated flow and that an extremely large pressure drop occurred in the vortices. In contrast to the two-dimensional simulation, three-dimensional inviscid simulations of the flow past a triangular column do not exhibit vortex shedding or a large pressure drop. Two shear layers develop from the trailing edges of the triangular column, and grid convergence to the experimental value of the drag coefficient is obtained. These validations confirm that the three-dimensional simulations are applicable for certain kinds of the flows around a body with sharp-edge separation; while, the two-dimensional simulations are invalid for the flow around a body with sharp-edge separation.

In chapter 3, the CFD analysis by the wall-modeled Cartesian cut-cell method is performed. The CFD analysis of the flow past a triangular column by wall-modeled Cartesian cut-cell method is performed and compare with the inviscid simulation. The result indicates that the inviscid simulation is sufficient to predict the flow which includes "sharp-edge separations". Also, numerical simulation of the flow around 30P30N three-element high-lift airfoil configuration is performed. The aerodynamic coefficients are agreed with the experimental results. Vortex structure of the outer-layer part of the turbulent boundary layer is formed on the suction side of the main element in the present study. Moreover, the unsteady movement of the separation point on the suction side of the flap is observed. These phenomena are not observed in the Euler simulation.

In chapter 4, coupled CFD analysis of the 1-DoF pitching motion of the reentry capsule is performed and the aerodynamic force model equation using the CFD result is proposed. Limit-cycle oscillation is represented in the fine-grid simulation. Axis of the vortex ring in the wake is displaced at pitch angle $\alpha = 0$, during the limit-cycle oscillation. The displacement causes the unsteady component of pitching moment around $\alpha = 0$. Pitching moment during the limit-cycle oscillation is decomposed into Fourier series. The amplitude of the third harmonics is larger than the dynamic component of the fundamental frequency. The model equation for the pitching moment which fully includes third harmonics is proposed. Present model equation reproduces the oscillation growing and limit-cycle oscillation simultaneously. Moreover, dynamic component of the unsteady aerodynamic work of the present model gives better estimate than conventional model equation by Hiraki.

The chapter 5 concludes the present study.

Contents

Acknowledgments **87**

List of Tables

List of Figures

Chapter 1

Introduction

1.1 Backgound of the present study

1.1.1 Computational grid in computational fluid dynamics

Computational fluid dynamics (CFD) is one of the most important tools of research and development in aerospace engineering. In tradition, boundary fit meshes are usually used in the CFD of aerospace engineering. Boundary fit mesh is effective to resolve the boundary layer on the wall.

Boundary fit mesh using a general curvilinear coordinate is introduced by Vinokur in 1974[2]. Before the implementation of the general curvilinear coordinate, the boundary fit grid which is made by the conformal map, and the Cartesian grid were used in aerospace engineering. However, the conformal map could not apply to the complex geometry which contains multiple curves, so that the object is limited to simple geometry. General curvilinear coordinate realizes the generation of boundary fitted mesh on the complex geometry which contains multiple curves. A flat computational cell made by general curvilinear coordinate is effective for reducing the number of computational cell in the Reynolds averaged Navier-Stokes (RANS) simulation which does not require to capture the small-scale eddies directly.

Cartesian mesh was mainly used in the multiphase flow containing phase interfaces and the external flow around the object with large deformation which is difficult to apply the boundary fitted mesh in the aspect of the mesh generation cost. In recent years,

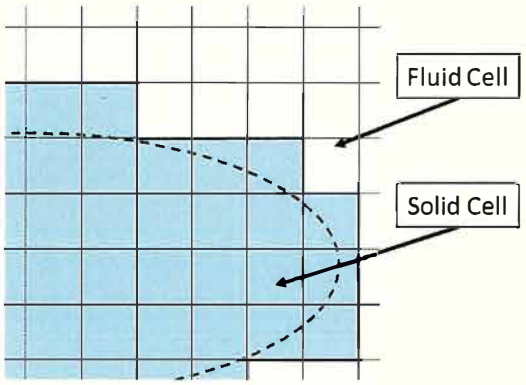

Fig. 1.1: Voxel method

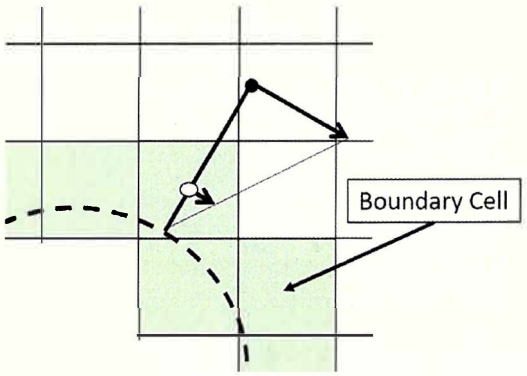

Fig. 1.2: Immersed boundary method

Cartesian mesh expands the range of the application with the increasing of the resource of the supercomputers and the development of the near-wall treatment.

1.1.2 Cartesian grid solver and object definition on the Cartesian grid

Cartesian grid solver detects the object (or phase interface) in the Cartesian grid. It is advantageous regarding grid generation cost and robustness. Volume of fluid (VOF) method[3] and level set method[4] are well-known methods that treat the phase interfaces of the multiphase flow. However, these methods treat the phase interface as the finite interface thickness (diffusive interface), rather than a sharp interface that much thinner than the grid width Δx. This treatment of the phase interface is effective for the stability of the simulation.

Cartesian cut-cell method[5, 6, 7], voxel method, and immersed boundary method[8, 9, 10] are typical Cartesian-grid methods using the sharp interface treatment. Voxel method represents the object shape as step-wise so that the object surface accords with the cell-interface (Fig. 1.1). Voxel method is easy to implement but it requires many computational cells to avoid the effect to the CFD of the step-wise wall treatment. On the other hand, immersed boundary method instead fixes conservative variables at the boundary cell to satisfy the boundary conditions; a boundary cell is a computational cell that includes an object surface (Fig. 1.2). The immersed boundary method does not satisfy the mass and energy conservation law in the boundary cells.

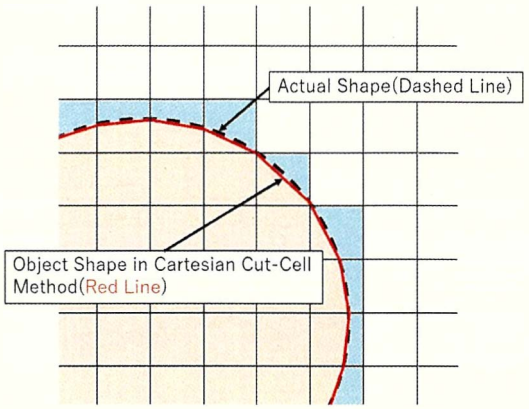

Fig. 1.3: Cartesian cut-cell method

Cartesian cut-cell method (Fig. 2.2) treats the object surface in a computational cell as a plane and sets wall flux vectors across the cut plane. Cartesian cut-cell method well follows the object surface rather than the voxel method, and conserves mass and energy.

In general, the Cartesian mesh is more difficult to resolve the boundary layer than the boundary fit mesh. Grid refinement techniques, such as the quadtree grid[11] or the building-cube method[12] achieve success in grid resolution in the boundary layer. However, those methods require an unstructured grid system that impairs the simplicity of computational codes. Furthermore, the non-smooth connection of discontinuous grid-scale of those method causes numerical dissipation. It makes difficult to achieve high order accuracy in space.

Cartesian mesh is advantageous to boundary fit mesh in the aspect of the robustly mesh generation from the "dirty" CAD data. Application range of the Cartesian grid is expandable using appropriate conservative equation and near-wall treatment.

1.1.3 Wall modeling in the unsteady flow simulation

Choi and Moin[13] estimate the number of total computational cell which is required in direct numerical simulation (DNS), wall-resolving large eddy simulation (WRLES) and wall-modeled LES (WMLES) are $N_{DNS} \sim Re^{37/14}$, $N_{WR} \sim Re^{13/7}$ and $N_{WM} \sim Re$ respectively. This increment of the total number of the computational cell is caused by the decreasing of the vortex scale with the increasing of the Reynolds number in the inner-layer part of the turbulent boundary layer which is about 10% of the turbulent boundary

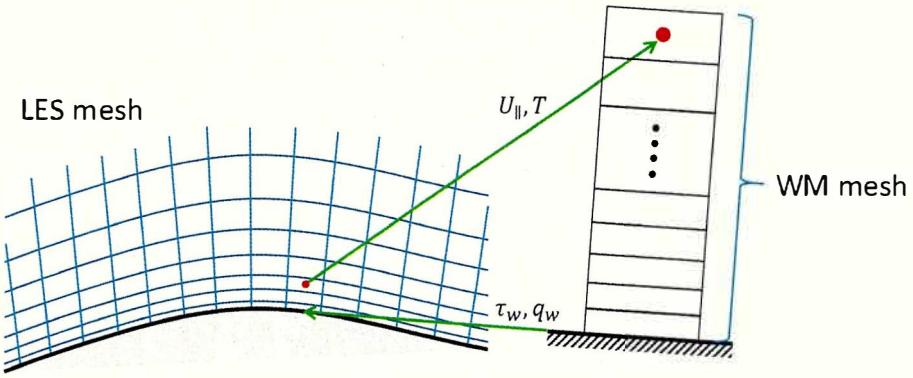

Fig. 1.4: Schematic of LES grid and WM grid

layer thickness. This fact shows the grid resolving of the high Reynolds number flows ($Re > 10^6$) without wall-modeling is unrealistic.

Wall-modeled LES is categorized into hybrid LES/RANS model and wall-stress model. Hybrid LES/RANS model switches to RANS equation in the boundary layer. Hybrid LES/RANS model is categorized into seamless model (Detached Eddy Simulation[14] DES) and zonal model (most of hybrid LES/RANS model[15]). Wall-stress model solves LES without non slip-wall condition and bring the wall-stress from the solution of the model equation. Wall-stress model is also categorized into math-based model (control theory[16], filter based[17]) and physics-based model using ordinary differential equation[18].

The shift of the velocity distribution in the log-layer that is called "log-layer mismatch" is reported by Nikitin *et al.* [14] and Kawai & Larson[18]. Other wall models[16, 17] are also suffered from this error that is caused by the mismatched estimation of the skin friction. Kawai & Larson[18] reveal the log-layer mismatch of the wall-stress-modeled LES depends on the location of the connection point of the LES and the wall-stress model. The wall-stress model requires the instantaneous LES values of two or more distant grid point from the wall to prevent the log-layer mismatch[18].

Wall-stress-modeled LES requires to resolve the outer-layer part of the turbulent boundary layer (Fig. 1.4), and the velocity distribution of wall-stress model agrees with that in turbulent boundary layer. Therefore, the wall-models do not appropriate for the laminar boundary layer.

In considerable high-Reynolds-number flows, the effect of the viscosity is negligible

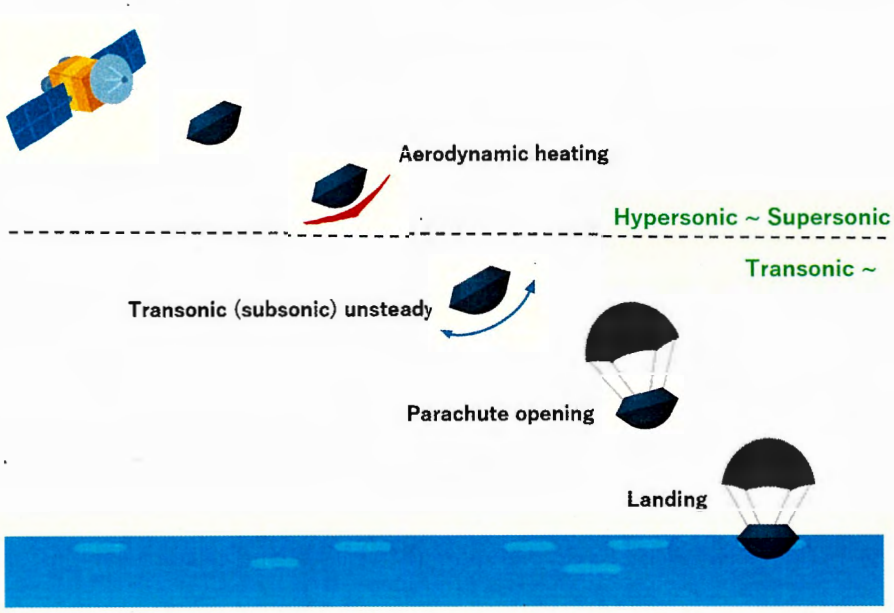

Fig. 1.5: Overview of atmospheric reentry

small rather than inertia. For this reason, inviscid numerical simulations of external flows by Euler equation[19, 20] or potential equation[21, 22] were presented since the dawn of the history of computational fluid dynamics. Computational cost of Euler simulations is less than Navier-Stokes simulations because Euler simulations do not require the grid resolution in the boundary layer. Inviscid simulations by Euler equation is still applicable to the prediction of the practical flows with the appropriate conditions.

1.1.4 Unsteady aerodynamics of the reentry capsule

Reentry capsule is essential for the development of space exploration. Reentry capsule is the only way for the return of the astronauts and specimens from outside of the earth after the retire of the space shuttle (Fig. 1.5).

Dynamic instability is one of the unsettled problems in reentry of the blunt-body capsule[23]. Reentry capsule is designed to keep stable during hypersonic flight. In contrast, reentry capsule falls into dynamic unstable in the transonic region or the subsonic region. The transonic instability may cause the failure to open the parachute in the worst case. Dynamically stable reentry during transonic condition before parachute opening is essential to the safe landing. Furthermore, stable parachute opening at low altitude in subsonic condition improves the accuracy of landing point owing to the reduction of the

surface wind effect.

Free-rotation test[24, 25, 26, 27] and free-flight[25, 28, 29] test are typical experiments for dynamic characteristics of the reentry capsule. Free-rotation test is a typical experiment using a wind tunnel. Free-rotation test is not able to reproduce the six degree-of-freedom (DoF) motion of the reentry capsule, but various data is obtained in free-rotation test in various flow conditions. Free-flight tests are conducted using the ballistic range or balloon. Free-flight test reproduces the 6-DoF motion of the reentry capsule, but the cost of this experiment is comparatively expensive in general.

Numerical simulations that attempt to predict the dynamic instability of the reentry capsule had been performed in fixed capsule[30, 31, 32] and forced oscillation[33, 34]. However, the interactions between the pitching motion and flow around capsule is not discussed sufficiently. Grid generation cost in each time step associated with using the boundary fit mesh makes difficult to perform coupled analysis.

Cartesian mesh does not require grid generation in each time step of the coupled analysis and is applicable to the coupled analysis with multiple objects in the different inertial systems which is difficult to treat by arbitrary Lagrangian-Eulerian (ALE) method[35]. Moreover, Cartesian mesh avoids the computational cost caused by hole-cutting on the overset grids[36].

1.2 Purpose of the present study and construction of the present thesis

The present study investigates the developability of the Cartesian grid solver especially Cartesian Cut-Cell method to the High Reynolds number flows. Application of the Euler equation to the sharp-edge separated flow is performed. Moreover, application of the wall-model to the Cartesian cut-cell method is performed.

Chapter 1 "Introduction" introduce the background and object of the present thesis.

Chapter 2 "Applicability of the Inviscid Simulations to the Flow around a Body with Sharp-Edge Separation using Cartesian Cut-Cell Method" assesses the applicability of the Euler simulation to the sharp-edge separated flows by the flow around a triangular column.

Chapter 3 "Applicability of the Wall-Modeled Cartesian Cut-Cell Method to the High Reynolds Number Flows" assesses the compatibility of the wall-model and Cartesian cut-cell method to the high Reynolds number flows. Furthermore, the result of the wall-modeled Navier-Stokes simulation and Euler simulation is compared in order to discuss the applicable limit of the Euler simulation.

Chapter 4 "Coupled Numerical Analysis of Three-Dimensional Unsteady Flow with Pitching Motion of Reentry Capsule" shows the coupled numerical analysis of flow and pitching motion of reentry capsule by inviscid Euler simulation. This chapter assesses the effect of the grid resolution of the wake to the pitching oscillation, additionally, the model of pitching moment which fully includes the third harmonics is proposed.

Chapter 5 "Conclusion" concludes the present thesis based on the preceding discussions.

Chapter 2

Applicability of the Inviscid Simulations to the Flow around a Body with Sharp-Edge Separation using Cartesian Cut-Cell Method

2.1 Introduction

Recently, computational methods using Cartesian grids have been receiving considerable attention [37, 12, 38]. These methods have advantages that can reduce computational costs and the time required to generate boundary-fitted meshes to object surfaces in the flow.

The Cartesian cut-cell method [5, 6, 7] and the immersed boundary method [8, 9, 10] are typical boundary treatments that use a Cartesian grid. The Cartesian cut-cell method treats the object surface in a computational cell as a plane and sets wall flux vectors normal to the cut plane. The immersed boundary method instead fixes conservative variables at the boundary cell to satisfy the boundary conditions; a boundary cell is a computational cell that includes a object surface. The immersed boundary method does not satisfy the mass conservation law in the boundary cells, while the Cartesian cut-cell method satisfies it. For this reason, the Cartesian cut-cell method is more precise than the immersed boundary method in general.

Columnar objects are popular structures in constructions or mechanical products.

High-Reynolds-number flows are frequently observed around constructions. Sharp-edge separation [39] often occurs in the flow around columnar objects. Consequently, the efficient prediction of the flow with sharp-edge separation is significant.

The grid resolution in the boundary layer causes an increase in the computational cost. Numerical simulations using the Cartesian grid with uniform interval require remarkable increase of the cost. Grid refinement techniques, such as the quadtree grid [11] or the building-cube method [12] achieve success in grid resolution in the boundary layer. However, those methods require an unstructured grid system that impairs the simplicity of a computational code. Furthermore, non-smooth connection of discontinuous grid-scale included in those methods makes it difficult to achieve high order accuracy in space.

The present study proposes another approach. The present study attempts to avoid the difficulties of grid resolution in the boundary layer by using an inviscid simulation. Inviscid simulations requires less computational cost than Navier-Stokes simulation with sufficient grid resolution in boundary layers. According to boundary-layer theory [40] and the perturbation method [41, 42], the solution of the external stream of boundary layer is provided by the solution of Euler equation. These theories are valid at the upstream side from the sharp edge or in flows without separation points. In the present study, an inviscid simulation is employed for the external stream of the boundary layer to a flow around a body with sharp-edge separation. At the downstream side from the sharp-edge, a shear layer forms along the streaklines from the trailing edge of the object. In a theoretical solution of Euler equation, a free shear layer is a slip surface across which the velocity is discontinuous. However, in a numerical simulations, a free shear layer has finite thickness owing to the artificial viscosity.

The present study formulates a hypothesis that the inviscid simulation predicts the aerodynamic force within sufficiently small error in practical applications when the aerodynamic force hardly depends on the Reynolds number. This hypothesis can not apply to the flows in which the separation point is not uniquely fixed, such as a flow around a circular column; because the separation point and drag depend on the Reynolds number.

The present study discuss the applicability of the inviscid simulation using the Cartesian cut-cell method. Numerical simulations of the flow past an NACA 0012 airfoil have

been performed as a verification problem for the Cartesian cut-cell code. In addition, numerical simulations of the flow past a triangular column have been performed to validate the hypothesis of the inviscid simulations to flows around a body with sharp-edge separation.

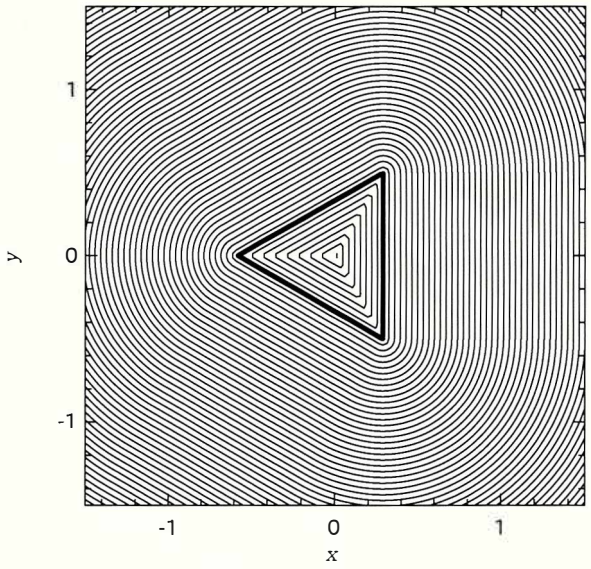

Fig. 2.1: Contour lines of the level set function around a triangular column.

2.2 Governing equations and simulation method

2.2.1 Definition of the object surface

The object surface is defined by following function ϕ:

$$\begin{array}{ll} \phi(x,y,z) > 0 & \text{in the air,} \\ \phi(x,y,z) = 0 & \text{on the object surface,} \\ \phi(x,y,z) < 0 & \text{in the object.} \end{array} \tag{2.1}$$

$$|\nabla\phi| = 1. \tag{2.2}$$

Variables x, y, z represent spatial Cartesian coordinates. Since the definition of ϕ is the same as that of the distance function in the level set method [4], this function is called the "level set function." Figure 2.1 shows the contour lines of the level set function of a triangular column. The level set function ϕ is given by continuous and piecewise-smooth elementary functions fitted the object surface in Fig. 2.1.

2.2.2 Cartesian cut-cell method

The Cartesian cut-cell method is a computational scheme that cuts the computational cells according to the object shape, as shown in Fig. 2.2. The Cartesian cut-cell method in the present study determines the positional relationship between the cut surfaces and the computational cells from the values of the level set function at each grid point, namely,

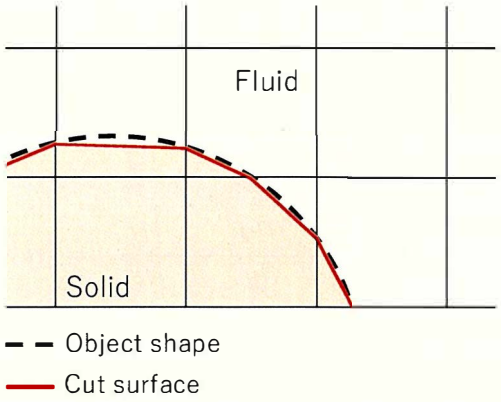

Fig. 2.2: Schematic of the Cartesian cut-cell method. The dotted line represents the object shape which is defined by level set function, and the red line represents the object shape which is reconstructed by the Cartesian cut-cell method.

each corner of the computational cell. The volume fraction in the computational cells and the surface fraction on the cell interfaces are calculated from the cutting pattern.

A fully three-dimensional Cartesian cut-cell method becomes complicated because of the many cutting patterns required. However, a computational cell cut by vertical columnar objects is the same as a two-dimensional calculation because the object shape is uniform in the vertical direction. Therefore, in the present study, the same evaluation method for volume and surface fractions has been applied to a three-dimensional calculation and a two-dimensional cut-cell calculation.

Some computational cells with small volume fractions, called "small cells," occur in the cut cells. The failure to satisfy the Courant-Friedrichs-Lewy (CFL) condition in a small cell causes instability in explicit schemes. Therefore, in the present study, the "cell merging" technique [5] has been used to avoid the instability caused by the small cells.

2.2.3 Governing equation

The governing equation is the compressible Euler equation. Conservation laws can be written in the following form.

$$\frac{\partial H\boldsymbol{Q}}{\partial t}+\frac{\partial H\boldsymbol{E}}{\partial x}+\frac{\partial H\boldsymbol{F}}{\partial y}+\frac{\partial H\boldsymbol{G}}{\partial z}=(\boldsymbol{n}\cdot\nabla H)\,\boldsymbol{\sigma}. \tag{2.3}$$

Here, H is the Heaviside function:

$$H(x,y,z)=\frac{1}{2}\{1+\mathrm{sgn}(\phi)\}=\begin{cases}1 & \text{in the air,}\\ 0 & \text{in the object.}\end{cases} \tag{2.4}$$

The Heaviside function is determined easily from the level set function, as indicated above. The vector $\boldsymbol{n}$ represents a unit normal vector directed outward from the object into the air. The scalar product $\boldsymbol{n}\cdot\nabla H$ is the Dirac delta function, which is defined in the direction normal to the surface of the object.

The variable $\boldsymbol{\sigma}$ on the right-hand side of Eq. (4.1) represents the wall flux vector (the interaction between the object and the air), which is directed into the air from the object:

$$\boldsymbol{\sigma}=\begin{pmatrix}0\\ pn_x\\ pn_y\\ pn_z\\ 0\end{pmatrix}. \tag{2.5}$$

Momentum exchange through the pressure is included, while mass transfer and energy exchange do not exist in the problems considered in the present paper.

The conserved quantities $\boldsymbol{Q}$, and the fluxes $\boldsymbol{E}$, $\boldsymbol{F}$, and $\boldsymbol{G}$ in Eq. (4.1) are defined as follows:

$$\boldsymbol{Q}=\begin{pmatrix}\rho\\ \rho u_x\\ \rho u_y\\ \rho u_z\\ e\end{pmatrix},\quad \boldsymbol{E}=\begin{pmatrix}\rho u_x\\ \rho u_x^2+p\\ \rho u_y u_x\\ \rho u_z u_x\\ e u_x+p u_x\end{pmatrix},\quad \boldsymbol{F}=\begin{pmatrix}\rho u_y\\ \rho u_x u_y\\ \rho u_y^2+p\\ \rho u_z u_y\\ e u_y+p u_y\end{pmatrix},\quad \boldsymbol{G}=\begin{pmatrix}\rho u_z\\ \rho u_x u_z\\ \rho u_y u_z\\ \rho u_z^2+p\\ e u_z+p u_z\end{pmatrix}. \tag{2.6}$$

The variable ρ is the density, u_x, u_y, and u_z are the components of the velocity, p is the pressure, and e is the total energy per unit volume:

$$e=\rho\epsilon+\frac{1}{2}\rho(u_x^2+u_y^2+u_z^2). \tag{2.7}$$

The internal energy per unit mass is given in the linear approximation as follows:

$$\epsilon = c_v T. \tag{2.8}$$

For the purposes of the present paper, air is considered to be an ideal gas, which satisfies the following equation of state:

$$p = \rho R T. \tag{2.9}$$

The following equations give the gas constant R and the specific heat at constant volume c_v using the molar mass M and specific heat ratio γ:

$$R = \frac{\mathcal{R}}{M}, \qquad c_v = \frac{R}{\gamma - 1}, \tag{2.10}$$

where $\mathcal{R}$ is the universal gas constant, and the specific heat at constant volume c_v is a constant. The speed of sound in air is given as follows:

$$a = \sqrt{\gamma R T}. \tag{2.11}$$

2.2.4 Generation of the simulation grid

The simulation domain consists of a uniform grid and a non-uniform grid. The Cartesian cut-cell method is applied in the uniform grid domain, which is placed at the center of the simulation domain. The non-uniform grid is used to reduce computational costs. A one-dimensional, non-uniform grid in xyz space is mapped onto a uniform grid in $\xi\eta\zeta$ space:

$$\xi = i\ \Delta\xi, \quad \eta = j\ \Delta\eta, \quad \zeta = k\ \Delta\zeta, \tag{2.12}$$

through the following monotone-increasing functions:

$$x = x(\xi), \quad y = y(\eta), \quad z = z(\zeta). \tag{2.13}$$

Here, the grid widths $\Delta\xi$, $\Delta\eta$, and $\Delta\zeta$ are set to unity for simplicity.

The following function is used to generate the non-uniform grid:

$$x = \exp\{(r-1)(\xi + c_1)\} + c_2(\xi + c_1)^3 + c_3(\xi + c_1)^2 + c_4(\xi + c_1) + c_5. \tag{2.14}$$

Here, the constant r is the rate of increase of the grid width; $r = 1.05$ is used in the present study. The coefficients c_1–c_5 are factors used to adjust the value at the connection

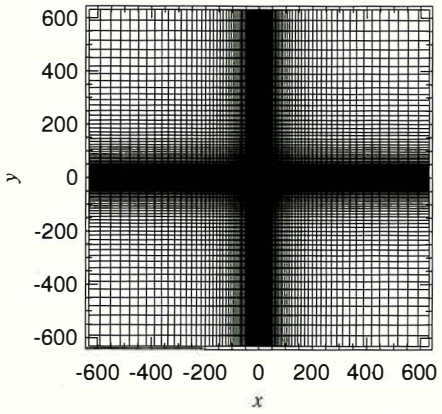

Fig. 2.3: Grid distribution of all simulation domain.

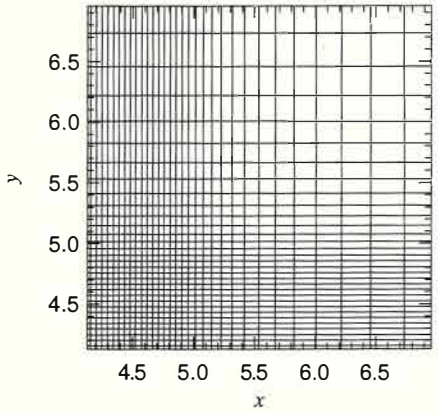

Fig. 2.4: Grid distribution around the connection point of uniform to non-uniform grid domain.

point between the uniform and non-uniform parts of the grid, and the conditions at the connection point are given as follows:

$$x(\xi_u) = x_u, \quad x_\xi(\xi_u) = \Delta x, \quad x_{\xi\xi}(\xi_u) = 0, \quad x_{\xi\xi\xi}(\xi_u) = 0. \tag{2.15}$$

The variable x_ξ indicates a derivative of x respects to ξ. The constants ξ_u and x_u are the number of grid points and the x coordinate at the connection point, respectively. The constant Δx is the grid width in the uniform grid domain. From Eq. (2.15), the coefficients c_1–c_5 are obtained as follows:

$$\begin{aligned} &c_1 = -\xi_u, \quad c_2 = -\frac{(r-1)^3}{6}, \quad c_3 = -\frac{(r-1)^2}{2}, \\ &c_4 = \Delta x - (r-1), \quad c_5 = x_u - 1. \end{aligned} \tag{2.16}$$

The non-uniform grids in the other directions are generated using similar equations. Figures 2.3 and 2.4 show the computational grid in the xy plane.

The conservation equation (4.1) can now be transformed into the following form using the one-dimensional, non-uniform grid as follows:

$$\frac{\partial H\boldsymbol{Q}}{\partial t} + \frac{1}{x_\xi}\frac{\partial H\boldsymbol{E}}{\partial \xi} + \frac{1}{y_\eta}\frac{\partial H\boldsymbol{F}}{\partial \eta} + \frac{1}{z_\zeta}\frac{\partial H\boldsymbol{G}}{\partial \zeta} = (\boldsymbol{n}\cdot\nabla H)\,\boldsymbol{\sigma}. \tag{2.17}$$

In the uniform grid domain, H is a function of x, y, z as shown in Eq. (4.2) and x_ξ is equal to constant Δx, while H is equal to unity and x_ξ is a derivativbe of Eq. (2.14) in the non-uniform grid domain.

The governing equation (2.17) is solved using a cell-centered finite volume method cubic cells in $\xi\eta\zeta$ space. The cell size in the present study is $2\Delta\xi \times 2\Delta\eta \times 2\Delta\zeta$.

2.2.5 Simulation method and discretization based on the finite volume method

The Heaviside function H in the first term on the left-hand side of Eq. (2.17) is replaced by the volume fraction α of the air in the computational cell. The volume fraction α is equal to unity in the non-uniform grid domain, and the volume fraction α in the uniform grid domain is given by

$$\alpha = \frac{1}{8\Delta x\,\Delta y\,\Delta z}\int_{z-\Delta z}^{z+\Delta z}\int_{y-\Delta y}^{y+\Delta y}\int_{x-\Delta x}^{x+\Delta x} H\,\mathrm{d}x\,\mathrm{d}y\,\mathrm{d}z. \tag{2.18}$$

Further, the flux term $H\boldsymbol{f}$, $H\boldsymbol{g}$, and $H\boldsymbol{h}$ of Eq. (2.17) is replaced by $\beta_x\boldsymbol{f}$, $\beta_y\boldsymbol{g}$, and $\beta_z\boldsymbol{h}$, respectively, at the cell interfaces. The surface fraction β_x, β_y, and β_z of the air are evaluated on the cell interfaces normal to x, y, and z-axis, respectively. The surface fraction β is equal to unity in the non-uniform grid domain, while in the uniform grid domain, it is given by

$$\begin{aligned}
\beta_x &= \frac{1}{4\Delta y\,\Delta z}\int_{z-\Delta z}^{z+\Delta z}\int_{y-\Delta y}^{y+\Delta y} H\,\mathrm{d}y\,\mathrm{d}z\,,\\
\beta_y &= \frac{1}{4\Delta x\,\Delta z}\int_{z-\Delta z}^{z+\Delta z}\int_{x-\Delta x}^{x+\Delta x} H\,\mathrm{d}x\,\mathrm{d}z\,,\\
\beta_z &= \frac{1}{4\Delta x\,\Delta y}\int_{y-\Delta y}^{y+\Delta y}\int_{x-\Delta x}^{x+\Delta x} H\,\mathrm{d}x\,\mathrm{d}y\,.
\end{aligned} \tag{2.19}$$

Further, the delta function $\boldsymbol{n}\cdot\nabla H$ on the right-hand side of Eq. (2.17) is replaced by the following equation:

$$\nabla H = \nabla\cdot(H\,\mathsf{I}) \simeq \frac{1}{8\Delta x\,\Delta y\,\Delta z}\int_{y-\Delta z}^{y+\Delta z}\int_{y-\Delta y}^{y+\Delta y}\int_{x-\Delta x}^{x+\Delta x}\nabla\cdot(H\,\mathsf{I})\,\mathrm{d}x\,\mathrm{d}y\,\mathrm{d}z \tag{2.20}$$

where I denotes the unit tensor of the second order. Applying Gauss' divergence theorem to the right-hand side of this equation, we obtain

$$\begin{aligned}
\nabla H \simeq \frac{1}{8\Delta x\,\Delta y\,\Delta z}\int_{\mathrm{c.i.}} H\,\mathrm{d}\boldsymbol{S} = {}& \boldsymbol{e}_x\frac{(\beta_x)_{x+\Delta x}-(\beta_x)_{x-\Delta x}}{2\Delta x}\\
&+\boldsymbol{e}_y\frac{(\beta_y)_{y+\Delta y}-(\beta_y)_{y-\Delta y}}{2\Delta y}\\
&+\boldsymbol{e}_z\frac{(\beta_z)_{z+\Delta z}-(\beta_z)_{z-\Delta z}}{2\Delta z}.
\end{aligned} \tag{2.21}$$

In Eq. (2.21), the symbol $\int_{\text{c.i.}}$ indicates the surface integral over the six cell interfaces of the cell cube, and $d\boldsymbol{S}$ indicates a surface element vector of each cell interface. The quantities $\boldsymbol{e}_x$, $\boldsymbol{e}_y$, and $\boldsymbol{e}_z$ are unit vectors in the coordinate directions. The delta function $\boldsymbol{n} \cdot \nabla H$ can be represented using Eq. (2.21) and

$$\boldsymbol{n} = \frac{\nabla H}{|\nabla H|} \tag{2.22}$$

as follows:

$$\begin{aligned} \boldsymbol{n} \cdot \nabla H \simeq \Bigg\{ & \left(\frac{(\beta_x)_{x+\Delta x} - (\beta_x)_{x-\Delta x}}{2\Delta x} \right)^2 \\ & + \left(\frac{(\beta_y)_{y+\Delta y} - (\beta_y)_{y-\Delta y}}{2\Delta y} \right)^2 \\ & + \left(\frac{(\beta_z)_{z+\Delta z} - (\beta_z)_{z-\Delta z}}{2\Delta z} \right)^2 \Bigg\}^{1/2} . \end{aligned} \tag{2.23}$$

This quantity gives the area of the object surface that is clipped by the computational cell. If the object surface does not cross the computational cell, the delta function $\boldsymbol{n} \cdot \nabla H$ automatically becomes zero. This approximation is formulated with second order accuracy.

The advection flux of the compressible Euler equation at the cell interface is calculated using the SLAU method [43]. The primitive variables on the cell interface to third-order accuracy are reconstructed using the MUSCL scheme [44] with the Van Albada limiter [45]. The velocity components are obtained using the modification of the MUSCL scheme proposed by [46]. Also, the time integration to second-order accuracy is calculated using the TVD Runge-Kutta method [47].

Table 2.1: Grid dependence of the maximum Mach number

	The maximum Mach number
Vassberg and Jameson, 2009[1]	0.6199
Coarse	0.6061
Medium	0.6082
Fine	0.6131
Extra Fine	0.6164

2.3 Numerical simulations of flow past an NACA 0012 airfoil

2.3.1 Simulation condition

Two-dimensional numerical simulations of the flow past an NACA 0012 airfoil are performed for verifying the simulation code. The angle of attack of the airfoil is zero. The shape of the NACA 0012 airfoil is defined by the following equation [48]:

$$y(x) = \pm\frac{0.12}{0.2}\left(0.2969\sqrt{x} - 0.1260x - 0.3516x^2 + 0.2843x^3 - 0.1015x^4\right). \tag{2.24}$$

The simulation domain in the x and y directions is 120 times larger than the chord length c. A uniform grid is used in the domain $-1.5c \leq x \leq 1.5c$ and $-0.5c \leq y \leq 0.5c$. The grid widths in this domain are $\Delta x = \Delta y$, where $\Delta x = 6c/1000$ (coarse grid), $4c/1000$ (medium grid), $2c/1000$ (fine grid), and $c/1000$ (extra fine grid).

The ambient fluid is assumed to be air. The upstream and downstream boundary conditions are given by using constant Riemann invariants [49], while the boundary conditions at $y = y_{max}$ and $y = y_{min}$ also are fixed values. The inflow Mach number is 0.5.

2.3.2 Simulation results

The maximum Mach number for each grid width is shown in Table 2.1. For an inviscid simulation using a boundary-fit mesh [1], it is 0.6199, while the maximum Mach number in the present simulation is 0.6164. The maximum Mach number obtained by refining the grid width in the present simulations approaches the reference value.

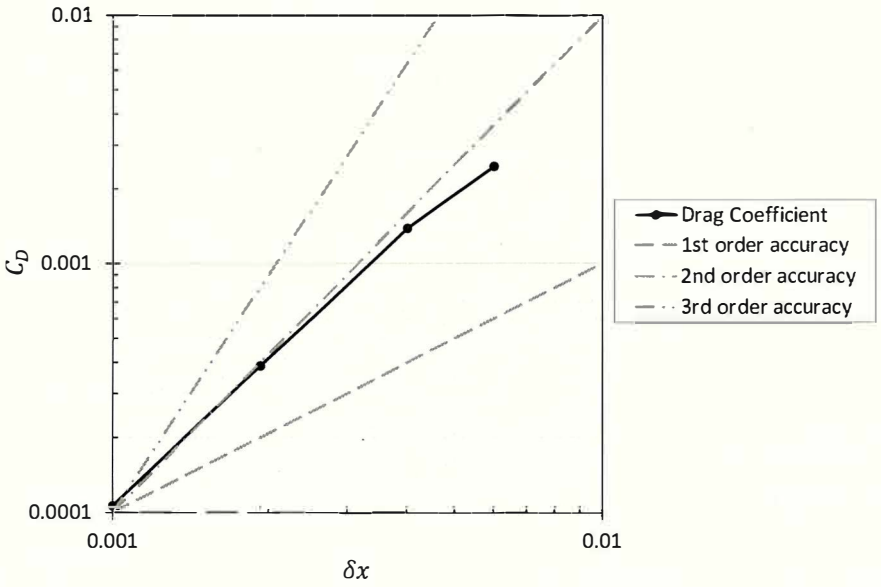

Fig. 2.5: Drag coefficient C_D on each grid width Δx. Plots represent the result of the present study. The dashed line denotes the first-order accuracy, the chain line denotes second-order accuracy, and the two-dotted chain line denotes third-order accuracy.

The drag coefficients obtained for each grid width are shown in Fig. 2.5.

$$C_D = \frac{2D}{\rho_0 u_0^2 c}. \tag{2.25}$$

Here, the subscript 0 indicates the value at the upstream boundary. The variable D represents the drag, which is assumed to be provided solely by the pressure. The local drag $f_{xi,j}$ on each computational cell is calculated from the following formula:

$$f_{xi,j} = p_{i,j} \left(\beta_{xi-1,j} - \beta_{xi+1,j} \right) \Delta y \Delta z. \tag{2.26}$$

Here, the subscripts $i-1$ and $i+1$ are the indices of the cell interfaces. The value of the drag acting on the object is obtained by applying Eq. (2.26) over the entire surface of the object. The drag coefficient is calculated from the steady value of the drag.

According to D'Alembert's paradox, the drag in an inviscid simulation is expected to vanish. Consequently, the drag coefficient shown in Fig. 2.5 is a measure of the numerical error of the method. It is expected to converge to zero as $\Delta x \to 0$. In the present study, the drag coefficient decreases as the grid width is refined, that is to say, grid convergence is obtained. The slope of double-logarithmic graph between each plot is 1.41 (Coarse–Medium), 1.83 (Medium–Fine), and 1.87 (Fine–Extra Fine). The value of

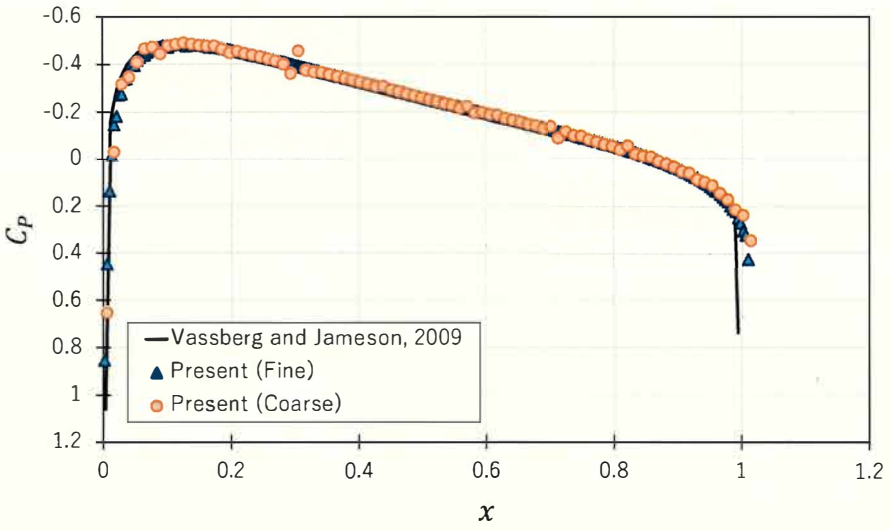

Fig. 2.6: Surface pressure C_P distribution on each grid width. The solid line represents the inviscid simulation [1], the circles represent the result of the present study (coarse grid), and the triangles represent the result of the present study (fine grid).

the slope increases as the grid width is refined, and it exhibits a tendency to converge to second order accuracy.

The pressure coefficient on the airfoil surface is calculated from the following equation:

$$C_P = \frac{p - p_0}{\frac{1}{2}\rho_0 u_0^2}. \tag{2.27}$$

The surface pressure distribution is shown in Fig. 2.6. The distribution obtained in present simulation agrees well with an inviscid analysis [1], except for the leading edge and the trailing edge. The pressure oscillations that occur in the coarse-grid simulation are mitigated in the fine grid simulation. The values of the pressure coefficient at the leading edge and the trailing edge approach the reference values as the grid width is refined.

2.4 Numerical simulations of flow past a triangular column

2.4.1 Simulation condition

The width of the simulation domain in the x and y directions is larger than $720d$, where d is the length of one side of the triangular column. A uniform grid in the domain $-4.62d \leq x \leq 4.62d$ and $-4.62d \leq y \leq 4.62d$ is employed. The height of the simulation domain along the axis of the column is $-6.28d \leq z \leq 6.28d$, almost the same as that used in a large eddy simulation (LES) computed by [50]. A uniform grid in the z (vertical) direction is used for the three-dimensional simulation. In addition, the two-dimensional calculation is performed as a three-dimensional calculation in which there is only one computational cell in the z direction

The grid width in the uniform grid domain is $\Delta x = \Delta y = \Delta z$, and the following three different grid widths are used: $\Delta x = 4.62\times10^{-2}d$ (coarse grid), $2.31\times10^{-2}d$ (medium grid), and $1.15 \times 10^{-2}d$ (fine grid).

The ambient fluid is assumed to be air. In the three-dimensional calculation, the initial velocity is selected to have the following distribution to promote three-dimensional disturbances:

$$u_x = u_{x0} + 0.01u_{x0} \cdot \sin\left(\frac{z}{z_{max}}\pi\right). \tag{2.28}$$

Here, the upstream Mach number is 0.3, and the constant z_{max} is half the width of the calculation domain in the z direction. This initial disturbance vanishes after the three-dimensional unsteady flow develops.

The time increment of $\Delta t = 2.0 \times 10^{-7}$s is used; therefore, the maximum Courant number in the fine grid simulation is approximately equal to 0.1.

The upstream boundary condition is fixed. The y and z components of the upstream velocity are set to zero. The downstream boundary condition is the free-outflow condition. The boundary conditions at $y = y_{max}$ and $y = y_{min}$ also are fixed values, and periodic boundary condition at $z = \pm z_{max}$ is used.

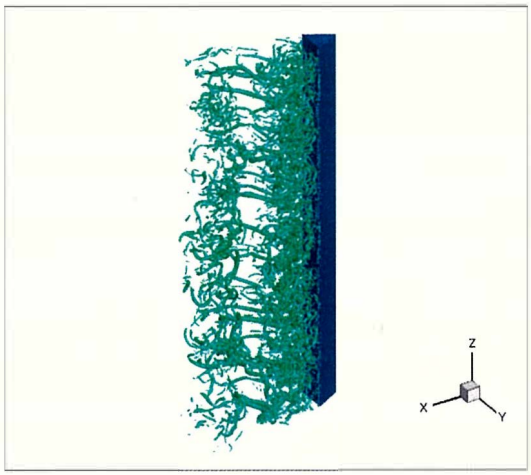

Fig. 2.7: Isosurfaces of the second invariant of the velocity-gradient tensor for the entire simulation domain of z.

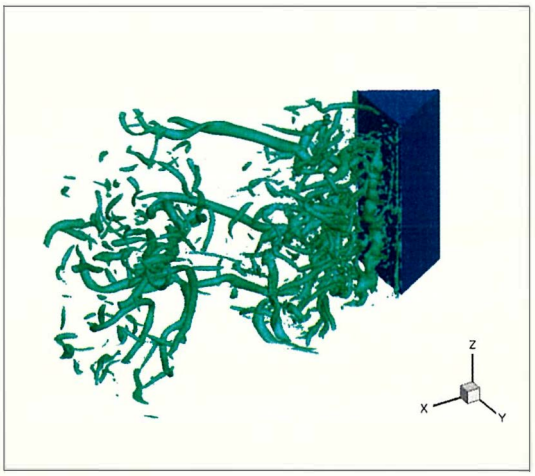

Fig. 2.8: Isosurfaces of the second invariant of the velocity-gradient tensor focusing on the central domain of z.

2.4.2 Simulation results

2.4.2.1 Three-dimensional visualization of flow structure

Figure 2.7 shows the isosurfaces of the second invariant of the velocity-gradient tensor in the uniform grid domain, and Fig. 2.8 shows an enlarged view of Fig. 2.7. These figures show that a complex vortex structure is formed in the wake of the triangular column. The vortex structure in the wake contains three-dimensional features that include longitudinal vortices.

2.4.2.2 Calculation of aerodynamic forces

Using the same method used in the case of the NACA 0012 airfoil, the local drag for each computational cell is calculated from Eq. (2.26). Similarly, the local lift f_y is calculated using the following formula in each computational cell:

$$f_{yi,j} = p_{i,j} \left(\beta_{yi,j-1} - \beta_{yi,j+1} \right) \Delta x \Delta z. \tag{2.29}$$

The value of the lift acting on the object is obtained by summing the values obtained from Eq. (2.29). The drag coefficient is defined by following equation:

$$C_D = \frac{2D}{\rho_0 u_0^2 d}. \tag{2.30}$$

The drag coefficient is calculated from the time-averaged value of the drag.

Table 2.2: Grid dependence of drag coefficient

	2D Simulation		3D Simulation	
	C_D	$\lvert C_D - C_{D,Exp}\rvert$	C_D	$\lvert C_D - C_{D,Exp}\rvert$
Coarse	1.601	0.276	1.476	0.151
Medium	1.858	0.533	1.161	0.164
Fine	2.100	0.775	1.334	0.009

Table 2.2 shows the drag coefficients obtained from the two-dimensional simulations and the three-dimensional simulations for each grid width. This table also shows the difference between the present simulations and the experimental value $C_{D,Exp} = 1.325$ obtained at Mach number 0.3 [51]. In the two-dimensional simulation, the drag coefficient increases as the grid width is refined. Contrary to expectations, the difference $|C_D - C_{D,Exp}|$ also increases as the grid width is refined.

In the three-dimensional simulation, the value of the drag coefficient is consistent with the experimental value despite the inviscid simulation. The drag coefficient first decreases and then increases slightly as the grid width is refined. The difference $|C_D - C_{D,Exp}|$ decreases as the grid width is refined, and it exhibits a tendency to converge to the experimental value.

2.4.2.3 Comparison of flow field structure

Figure 2.9 shows the flow field around the triangular column, as obtained from the two-dimensional simulation using the fine grid. The color contours show the pressure, and the vectors show the velocity. Vortex shedding accompanied by a markedly accelerated flow and an extremely large pressure drop occurs successively at the two trailing edges of the triangular column. These vortices form a von Kármán's vortex street in the wake. The velocities in the accelerated flow are appreciably greater than the upstream velocity, and the large pressure drop in the vortices behind the column causes an increase in the drag.

Figure 2.10 shows the flow field around the triangular column, as obtained from the three-dimensional simulation using the fine grid. In contrast to the two-dimensional simulations, the trailing edges of the column generate two shear layers behind the column in the three-dimensional simulations, and vortex streets are formed in the wake by rolling

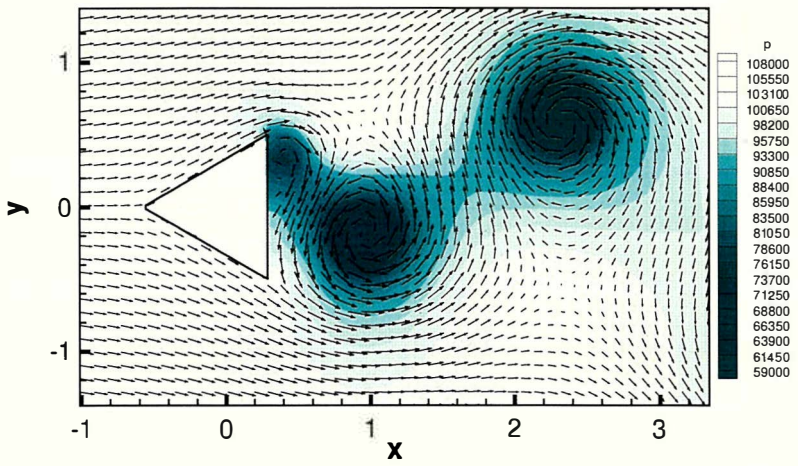

Fig. 2.9: Flow field in two-dimensional simulation; color counters show the pressure, and the vectors show the velocity.

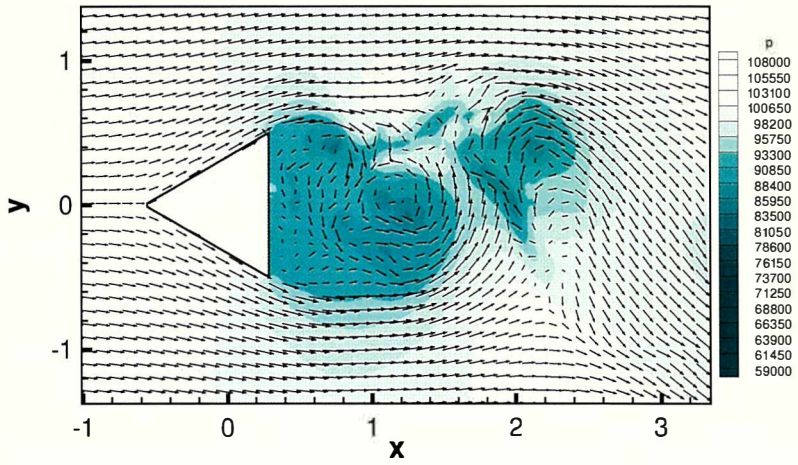

Fig. 2.10: Flow field in a cross section of the three-dimensional simulation; color counters show the pressure, and the vectors show the velocity.

up of the shear layers. Also, the pressure between the two shear layers is higher than that in Fig. 2.9; since the pressure drop in the wake is moderate in comparison to the two-dimensional calculation, the drag is reduced.

The formation of shear layers in the wake has also been reported in experiments in which the Reynolds number $Re = 520$ [52], Re ranges from 2.9×10^3 to 1.16×10^4 [50], and the LES in which Re ranges from 2.9×10^3 to 1.16×10^5 [50]. The flow pattern of Fig. 2.10 is similar to that of these experiments and LES. The results shown in Table 2.2 and Fig. 2.10 indicate that the three-dimensional simulations reproduce the major parts of the real flows. These comparisons validate the inviscid simulations for certain kinds of

flows around a body with sharp-edge separation.

2.4.2.4 Characteristic frequencies of lift and drag fluctuations

The power spectra of the fluctuations in the drag and the lift are obtained using a fast Fourier transform (FFT) using the spectrum analysis software "SPCANA Ver. 4.92." The drag and lift histories from the fine grid simulations are used for the spectrum analysis, with 8192 data points sampled at 50kHz. Figure 2.11 shows the power spectra of fluctuations in the drag and the lift.

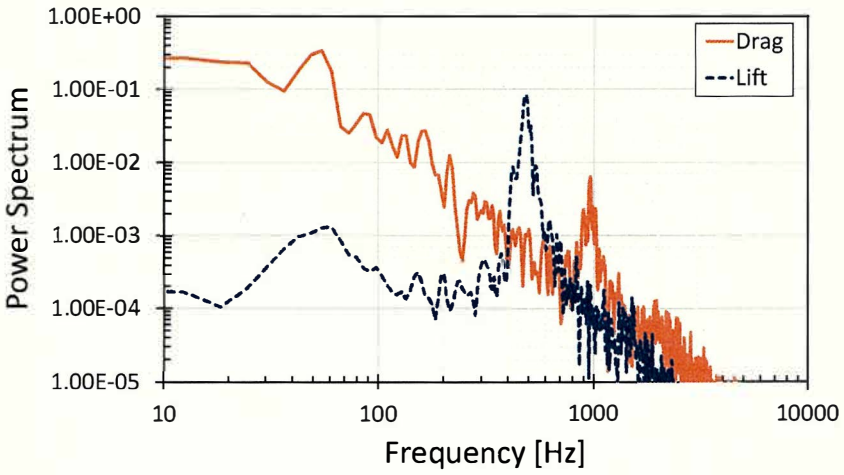

Fig. 2.11: Power spectra of fluctuations in the drag (solid line) and lift (dotted line).

Each power spectrum has two major peaks, which are at a high frequency and a low frequency. For the lift, the peak frequencies are 482 and 67.0Hz, while for the drag they are 964 and 67.0Hz. Note that the higher frequency in the drag spectrum is double that of the high frequency in the lift spectrum. Also note that the low frequency peak in the spectrum of drag fluctuations is stronger than the high frequency peak of drag.

The Strouhal number is calculated using the characteristic frequency of the lift fluctuations at $f = 482$Hz:

$$St = \frac{fd}{u_{x0}} = 0.201. \tag{2.31}$$

Table 2.3 shows the Strouhal numbers from the present simulations, from experiments [52, 50], and from the LES [50]. The Strouhal numbers from the experiments and from the LES are close to 0.2, and the Strouhal number from the present simulation matches these values.

Table 2.3: Strouhal number of the triangular column

		Re	St
Present	(Inviscid)	–	0.201
Agrwal *et al.* [52]	(Experiment)	520, 1.04×10^3	0.20, 0.197
Yagmur *et al.* [50]	(Experiment)	$2.9 \times 10^3 - 1.16 \times 10^4$	$0.211 - 0.225$
	(LES)	$2.9 \times 10^3 - 1.16 \times 10^5$	$0.214 - 0.230$

2.4.2.5 Correlation between the oscillations of the two shear layers and fluctuations in the drag

The wake of the triangular column in Fig. 2.10 is sandwiched between two free shear layers. The distance Δ_s between the two shear layers (i.e., the width of the wake) is given by

$$\Delta_s = \int_{-\infty}^{\infty} \left[1 - \frac{\min\{u_{x0}, \max(u_x, 0)\}}{u_{x0}} \right] dy. \tag{2.32}$$

This formula follows the displacement thickness of the boundary layer. The second term on the right-hand side of Eq. (2.32), the fast flow near the shear layers is rounded down to u_0, and the backflow in the wake is rounded up to zero. The width of the wake is calculated at $x = 0.565d$.

The correlation coefficient between the fluctuations in the drag and the width of the wake is -0.899, which represents a strong negative correlation. This indicates that the slow fluctuations in the drag and lift are caused by fluctuations in the width of the wake.

2.5 Conclusions

The applicability of inviscid simulations to real flows is discussed using the Cartesian cut-cell method. The inviscid simulation is employed for external stream of the boundary layer theory. The inviscid simulation requires less computational cost than Navier-Stokes simulation with sufficient grid resolution in boundary layer. The inviscid simulation is useful if it predicts aerodynamic force within sufficiently small error in practical applications. We exclude flows in which aerodynamic force remarkably depend on Reynolds number as well as flows in which separation points depend on Reynolds number.

For verifying simulation code, numerical simulations of the flow past an NACA 0012 airfoil are performed, and grid convergence of the maximum Mach number, drag coefficient, and surface pressure distribution are confirmed.

For validating the applicability of inviscid simulation, numerical simulations of the flow past a triangular column are performed. The drag coefficients calculated from the two-dimensional simulations are greater than those obtained from a reference experiment [51]. Contrary to expectations, the drag from these simulations increases as the grid width is refined. In these simulations, vortex shedding accompanied by a markedly accelerated flow and an extremely large pressure drop occurs in the vortices.

For the three-dimensional simulations, even though they are inviscid calculations, the difference between the calculated and reference experimental values of the drag coefficient is less than 1%. The difference also decreases as the grid width is refined, i.e., grid convergence is confirmed. The trailing edges of the triangular column generate two shear layers behind the column. Subsequently, a vortex street is formed in the wake by rolling up of the shear layers. The same flow structure has been observed in experiments [52, 50]. These results indicate that the present inviscid simulation reproduces the main parts of the real phenomena.

The major characteristic frequencies of the lift and the drag fluctuations are calculated using FFT analysis. The characteristic frequency of the lift match the frequency of von Kármán's vortex, as obtained in both the experiments [52, 50] and the LES [50]. Moreover, the slow fluctuations in the drag match the fluctuations in the width of the wake (i.e.,

the distance between the two shear layers).

These validations confirm that the three-dimensional inviscid simulations provide valid representations of certain kinds of flows around a body with sharp-edge separation as well as flows without separations. However, two-dimensional inviscid simulations are invalid for the flows that contain flow separation. They predict extremely large pressure drops in the vortices, which do not occur in either the three-dimensional simulations or the experiments.

The present study reveals limitation of the two-dimensional inviscid simulation and the applicability of the three-dimensional inviscid simulation to the flows around a body with sharp-edge separation. It needs further discussion of extent of the applicability of the three-dimensional inviscid simulation. Since the inviscid simulations do not require a fine grid to represent the boundary layer, the inviscid simulation by using the Cartesian cut-cell method is expected to evolve as a three-dimensional simulation tool within its applicable extent of problems.

Chapter 3

Applicability of the Wall-Modeled Cartesian Cut-Cell Method to the High Reynolds Number Flows

3.1 Introduction

High Reynolds number flows $Re \gtrsim 10^6$ frequently appear in the aerodynamic design of aircrafts and spacecrafts. In the computational fluid dynamics (CFD), Reynolds-averaged Navier–Stokes (RANS) simulation achieves remarkable success in steady flows. However, RANS simulation is difficult to apply to unknown unsteady flows. Large eddy simulations (LESs) are rather reliable in simulations of unknown unsteady flows.

In the turbulent boundary layer of $Re \gtrsim 10^6$ flows, LESs struggle to satisfy the sufficient grid resolution requirement due to the vortex scale decreasing in the inner layer of the turbulent boundary layer, which is about 10% of the turbulent boundary layer thickness. Choi and Moin [13] estimated that the total number of the computational grid required in a wall-resolved LES is proportional to $Re^{13/7}$.

The wall-stress model using one-dimensional equations in wall-normal coordinates for turbulence boundary layer was introduced by Kawai and Larson [18, 53, 54]. This model yields accurate wall shear stress and heat flux using instantaneous values from the LES. Shear stress and heat flux are provided to the LES in the form of flux across the wall in this model.

The Cartesian cut-cell method [5, 6, 7] subdivides the object surface into small flat

planes inside the cubical computational cells. In other words, these cells are divided by small cut planes into the fluid side and the object side. The interaction between the object and the fluid is given by wall flux vectors across the cut plane. Due to this sharp interface treatment and the robust grid generation of the Cartesian mesh, the Cartesian cut-cell method is one of the most promising methods in CFD. However, the Cartesian cut-cell method and other Cartesian mesh solvers struggle to satisfy the required grid resolution for boundary layers because rectangular cells with an extremely large aspect ratio used in boundary fitted mesh are not available with these methods. To overcome this difficulty, an appropriate near-wall treatment is required. The wall-stress model by Kawai and Larson is expected to be one of the most compatible wall treatment techniques with the Cartesian cut-cell method.

The present study performed numerical simulations of the flow past a triangular column and 30P30N high-lift airfoil configuration using the Cartesian cut-cell method with the wall-stress model. The numerical results of the present study revealed the prediction capability of the wall-stress model to the Cartesian cut-cell simulation of unsteady flows.

3.2 Governing Equation and Simulation Method

3.2.1 Governing Equation

The governing equation is the compressible Navier–Stokes equation. Conservation laws can be written in the following form:

$$\frac{\partial \boldsymbol{Q}}{\partial t} + \frac{\partial (\boldsymbol{E}_{\mathrm{a}} - \boldsymbol{E}_{\mathrm{d}})}{\partial x} + \frac{\partial (\boldsymbol{F}_{\mathrm{a}} - \boldsymbol{F}_{\mathrm{d}})}{\partial y} + \frac{\partial (\boldsymbol{G}_{\mathrm{a}} - \boldsymbol{G}_{\mathrm{d}})}{\partial z} = 0. \tag{3.1}$$

The conserved quantities $\boldsymbol{Q}$; the advection fluxes $\boldsymbol{E}_{\mathrm{a}}$, $\boldsymbol{F}_{\mathrm{a}}$, and $\boldsymbol{G}_{\mathrm{a}}$; and the viscous and conductive fluxes $\boldsymbol{E}_{\mathrm{d}}$, $\boldsymbol{F}_{\mathrm{d}}$, and $\boldsymbol{G}_{\mathrm{d}}$ in Equation (4.1) are defined as follows:

$$
\begin{aligned}
\boldsymbol{Q} &= \begin{pmatrix} \rho \\ \rho u_x \\ \rho u_y \\ \rho u_z \\ e \end{pmatrix}, \quad
\boldsymbol{E}_{\mathrm{a}} = \begin{pmatrix} \rho u_x \\ \rho u_x^2 + p \\ \rho u_y u_x \\ \rho u_z u_x \\ e u_x + p u_x \end{pmatrix}, \quad
\boldsymbol{F}_{\mathrm{a}} = \begin{pmatrix} \rho u_y \\ \rho u_x u_y \\ \rho u_y^2 + p \\ \rho u_z u_y \\ e u_y + p u_y \end{pmatrix}, \quad
\boldsymbol{G}_{\mathrm{a}} = \begin{pmatrix} \rho u_z \\ \rho u_x u_z \\ \rho u_y u_z \\ \rho u_z^2 + p \\ e u_z + p u_z \end{pmatrix}, \\
\boldsymbol{E}_{\mathrm{d}} &= \begin{pmatrix} 0 \\ \tau_{xx} \\ \tau_{yx} \\ \tau_{zx} \\ u_x \tau_{xx} + u_y \tau_{yx} + u_z \tau_{zx} - q_x \end{pmatrix}, \quad
\boldsymbol{F}_{\mathrm{d}} = \begin{pmatrix} 0 \\ \tau_{xy} \\ \tau_{yy} \\ \tau_{zy} \\ u_x \tau_{xy} + u_y \tau_{yy} + u_z \tau_{zy} - q_y \end{pmatrix}, \\
\boldsymbol{G}_{\mathrm{d}} &= \begin{pmatrix} 0 \\ \tau_{xz} \\ \tau_{yz} \\ \tau_{zz} \\ u_x \tau_{zx} + u_y \tau_{yz} + u_z \tau_{zz} - q_z \end{pmatrix},
\end{aligned}
\tag{3.2}
$$

where ρ is the density; u_x, u_y, and u_z are the components of the velocity; p is the pressure; and e is the total energy per unit volume. The variables $\boldsymbol{\tau}$ and $\boldsymbol{q}$ are the stress tensor and heat flux, respectively:

$$
\begin{aligned}
\tau_{xx} &= \frac{2}{3}\mu \left(2\frac{\partial u_x}{\partial x} - \frac{\partial u_y}{\partial y} - \frac{\partial u_z}{\partial z} \right), \\
\tau_{yy} &= \frac{2}{3}\mu \left(2\frac{\partial u_y}{\partial y} - \frac{\partial u_z}{\partial z} - \frac{\partial u_x}{\partial x} \right), \\
\tau_{zz} &= \frac{2}{3}\mu \left(2\frac{\partial u_z}{\partial z} - \frac{\partial u_x}{\partial x} - \frac{\partial u_y}{\partial y} \right), \\
\tau_{xy} &= \tau_{yx} = \mu \left(\frac{\partial u_x}{\partial y} + \frac{\partial u_y}{\partial x} \right), \\
\tau_{yz} &= \tau_{zy} = \mu \left(\frac{\partial u_y}{\partial z} + \frac{\partial u_z}{\partial y} \right), \\
\tau_{zx} &= \tau_{xz} = \mu \left(\frac{\partial u_z}{\partial x} + \frac{\partial u_x}{\partial z} \right).
\end{aligned}
\tag{3.3}
$$

$$
\begin{aligned}
q_x &= -\frac{1}{\gamma - 1}\frac{\mu}{Pr}\frac{\partial a^2}{\partial x}, \\
q_y &= -\frac{1}{\gamma - 1}\frac{\mu}{Pr}\frac{\partial a^2}{\partial y}, \\
q_z &= -\frac{1}{\gamma - 1}\frac{\mu}{Pr}\frac{\partial a^2}{\partial z},
\end{aligned}
\tag{3.4}
$$

a is the speed of sound; μ is the viscosity obtained by Sutherland's law; and the Prandtl number Pr is 0.72.

The product of Equation (4.1) and the Heaviside function $H(x, y, z)$ is reduced to

$$\begin{aligned}\frac{\partial H\boldsymbol{Q}}{\partial t} + \frac{\partial H(\boldsymbol{E}_\mathrm{a} - \boldsymbol{E}_\mathrm{d})}{\partial x} + \frac{\partial H(\boldsymbol{F}_\mathrm{a} - \boldsymbol{F}_\mathrm{d})}{\partial y} + \frac{\partial H(\boldsymbol{G}_\mathrm{a} - \boldsymbol{G}_\mathrm{d})}{\partial z} \\ = \frac{\partial H}{\partial x}(\boldsymbol{E}_\mathrm{a} - \boldsymbol{E}_\mathrm{d}) + \frac{\partial H}{\partial y}(\boldsymbol{F}_\mathrm{a} - \boldsymbol{F}_\mathrm{d}) + \frac{\partial H}{\partial z}(\boldsymbol{G}_\mathrm{a} - \boldsymbol{G}_\mathrm{d}).\end{aligned} \tag{3.5}$$

This equation extends the simulation domain that includs the object, where the Heaviside function $H(x, y, z)$ gives $H = 1$ in air and $H = 0$ in the object. The Heaviside function is treated as a generalized function [55] because it includes discontinuity at the object surface. Considering the relation $\nabla H = |\nabla H|\, \boldsymbol{n}$, we obtain the following equation.

$$\frac{\partial H\boldsymbol{Q}}{\partial t} + \frac{\partial H(\boldsymbol{E}_\mathrm{a} - \boldsymbol{E}_\mathrm{d})}{\partial x} + \frac{\partial H(\boldsymbol{F}_\mathrm{a} - \boldsymbol{F}_\mathrm{d})}{\partial y} + \frac{\partial H(\boldsymbol{G}_\mathrm{a} - \boldsymbol{G}_\mathrm{d})}{\partial z} = |\nabla H|\, \boldsymbol{\sigma}. \tag{3.6}$$

The vector $\boldsymbol{n}$ represents a unit normal vector directed outward from the object into the air. The variable $\boldsymbol{\sigma}$ on the right-hand side of Equation (3.6) represents the wall flux vector (the interaction between the object and the air), which is directed from the object into the air. Considering the boundary condition $\boldsymbol{u} \cdot \boldsymbol{n} = 0$ at the object surface, $\boldsymbol{\sigma}$ is reduced to the following form:

$$\boldsymbol{\sigma} = \begin{pmatrix} 0 \\ pn_x - \tau_{xx}n_x - \tau_{xy}n_y - \tau_{xz}n_z \\ pn_y - \tau_{yx}n_x - \tau_{yy}n_y - \tau_{yz}n_z \\ pn_z - \tau_{zx}n_x - \tau_{zy}n_y - \tau_{zz}n_z \\ 0 \end{pmatrix} \simeq \begin{pmatrix} 0 \\ pn_x - \tau_w b_x \\ pn_y - \tau_w b_y \\ pn_z - \tau_w b_z \\ 0 \end{pmatrix}. \tag{3.7}$$

The vector $\boldsymbol{b}$ is the stream-wise unit vector parallel to the wall. The scalar value τ_w of the wall shear stress is obtained by the wall-stress model. Wall flux of mentum through the pressure and the shear stress are included, while wall flux of mass and energy do not exist in the problems considered here.

The governing equation (3.6) is solved using a cell-centered finite volume method. The Heaviside function H in the time derivative term in Equation (3.6) is replaced by the volume fraction of air in the cell, and H in space derivative terms in Equation (3.6) is replaced by the area fractions β_x, β_y, and β_z of air in each cell interface. We replace

$|\nabla H|$ into the following approximation:

$$|\nabla H| \simeq \left\{ \left(\frac{(\beta_x)_{x+\Delta x/2} - (\beta_x)_{x-\Delta x/2}}{\Delta x} \right)^2 + \left(\frac{(\beta_y)_{y+\Delta y/2} - (\beta_y)_{y-\Delta y/2}}{\Delta y} \right)^2 + \left(\frac{(\beta_z)_{z+\Delta z/2} - (\beta_z)_{z-\Delta z/2}}{\Delta z} \right)^2 \right\}^{1/2}, \tag{3.8}$$

where Δx, Δy, and Δz are the grid width. The finite volume approximation of $|\nabla H|\ \Delta x\ \Delta y\ \Delta z$ gives the area of the small cut-plane in the computational cell.

The advection flux at the cell interface is calculated using the Simple Low-dissipation AUSM (SLAU) scheme [43]. The primitive variables on the cell interface are reconstructed using Monotonic Upstream-centered Scheme for Conservation Laws (MUSCL) of the fifth-order accuracy [56]. The velocity components are obtained using the modification of the MUSCL scheme proposed by Thornber [46]. The time integration to second-order accuracy is calculated using the Total Variation Diminishing (TVD) Runge–Kutta method [47].

3.2.2 Wall-Stress Model

The wall-stress model by Kawai and Larson [18, 53, 54] for the turbulent boundary layer was used in the present study. Stream-wise momentum and the total energy conservation equation of the wall-stress model are written in the following ordinary differential equations in the local wall-normal coordinate η:

$$\frac{d}{d\eta}\left[(\mu + \mu_{t,\mathrm{wm}}) \frac{dU_\parallel}{d\eta} \right] = 0, \tag{3.9}$$

$$\frac{d}{d\eta}\left[(\mu + \mu_{t,\mathrm{wm}}) U_\parallel \frac{dU_\parallel}{d\eta} + c_p \left(\frac{\mu}{Pr} + \frac{\mu_{t,\mathrm{wm}}}{Pr_{t,\mathrm{wm}}} \right) \frac{dT}{d\eta} \right] = 0, \tag{3.10}$$

where $U_\parallel$ is the wall-parallel velocity component. Constants $Pr = 0.72$ and $Pr_{t,\mathrm{wm}} = 0.90$ are the Prandtl number and turbulent Prandtl number, respectively. The solution of the wall-stress model equations shows the averaged velocity and the averaged temperature distributions in the inner-layer part of the turbulent boundary layer. The turbulent eddy viscosity in the wall-stress model $\mu_{t,\mathrm{wm}}$ is obtained using the following formula:

$$\mu_{t,\mathrm{wm}} = \kappa \rho \eta \sqrt{\frac{\tau_w}{\rho}} D, \tag{3.11}$$

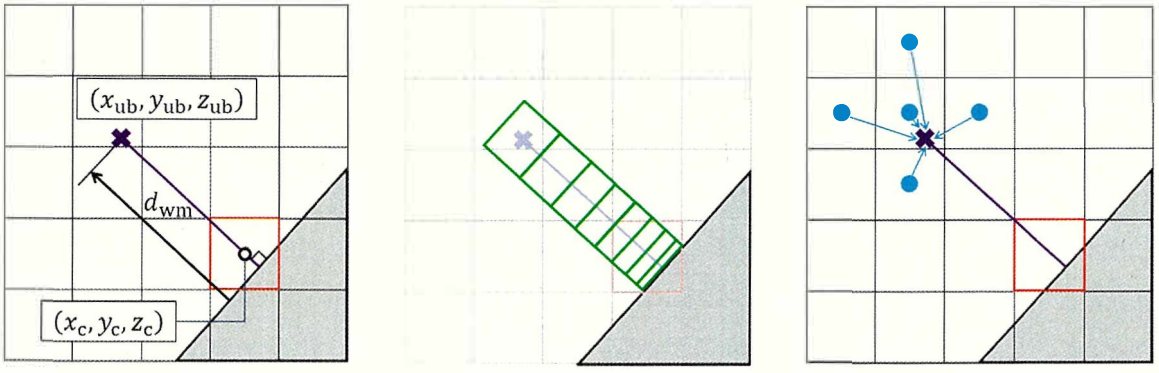

(a) Define the upper bound of the wall-stress model mesh using the wall distance d_{wm}.

(b) Generate the one-dimensional mesh for the wall-stress model that is independent of the Cartesian cut-cell mesh.

(c) Interpolate $U_{\parallel}$ and T to the upper boundary value of the wall-stress model using inverse distance weighting.

Fig. 3.1: Overview of the application of the wall-stress model to the Cartesian cut-cell method.

$$D = \left[1 - \exp(-y^+/A^+)\right]^2. \tag{3.12}$$

The von Kármán constant is $\kappa = 0.41$, and A^+ is a constant that equals 17. The velocity scale $u_\tau = \sqrt{\tau_w/\rho}$ is estimated by the instantaneous wall shear stress and density. The dimensionless wall distance y^+ in Equation (3.12) is defined as:

$$y^+ = \frac{\rho \eta u_\tau}{\mu}. \tag{3.13}$$

The boundary value problem of the wall-stress model Equations (3.9) and (3.10) are discretized using the one-dimensional finite volume method and solved by the Thomas algorithm. Boundary values at $\eta = \eta_{max} = d_{wm}$ are determined from the instantaneous value of the CFD analysis (Figure 3.1a).

A schematic of the application of the wall-stress model to the Cartesian cut-cell method is shown in Figure 3.1. An overview of the implementation is provided as follows:

a. The upper bound of the wall-stress model mesh is set on the wall-normal line passing through a CFD cell center (x_c, y_c, z_c) that includes the cut-plane by the object. The upper bound is placed at distance d_{wm} from the wall. The distance d_{wm} corresponds to $y^+ \sim 300$. The location of the upper bound (x_{ub}, y_{ub}, z_{ub}) of the wall-stress

model in the CFD domain is decided as follows:

$$x_{\mathrm{ub}} = x_{\mathrm{c}}+(d_{\mathrm{wm}}-\varphi_{\mathrm{c}})n_x, \quad y_{\mathrm{ub}} = y_{\mathrm{c}}+(d_{\mathrm{wm}}-\varphi_{\mathrm{c}})n_y, \quad z_{\mathrm{ub}} = z_{\mathrm{c}}+(d_{\mathrm{wm}}-\varphi_{\mathrm{c}})n_z, \tag{3.14}$$

where φ_{c} denotes the distance from the wall to the CFD cell center $(x_{\mathrm{c}},\ y_{\mathrm{c}},\ z_{\mathrm{c}})$.

b. The one-dimensional non-uniform mesh for the wall-stress model is generated from the wall to the upper bound. The wall-stress model mesh is generated using the following formula:

$$\eta = \exp\left[(r_{\mathrm{wm}} - 1)\,(j_{\mathrm{wm}} + c_1)\right] + c_2, \tag{3.15}$$

where j_{wm} denotes the cell number from the wall; $r_{\mathrm{wm}} = 1.1$ denotes the rate of the increment of the grid distancing between neighboring grid points. The grid distancing increases by 10% between neighboring grid points. Constants c_1 and c_2 is decided to satisfy the following conditions:

$$\eta = 0 : \text{ at the wall } (j_{\mathrm{wm}} = 0), \quad \eta = d_{\mathrm{wm}} : \text{ at the upper bound } (j_{\mathrm{wm}} = 80). \tag{3.16}$$

c. The upper boundary values $U_{\parallel}$ and T are decided by inverse distance weighted interpolation using instantaneous values of the neighbor cell-center of the Cartesian cut-cell simulation as follows:

$$Q = \frac{\sum_{i=1}^{n} w_i Q_i}{\sum_{i=1}^{n} w_i}, \tag{3.17}$$

$$w_i = \frac{1}{\sqrt{(x_i - x_{\mathrm{ub}})^2 + (y_i - y_{\mathrm{ub}})^2 + (z_i - z_{\mathrm{ub}})^2}}. \tag{3.18}$$

The wall boundary condition of the wall-stress model equations is the non-slip and adiabatic wall in the present study.

d. Wall-stress model Equations (3.9) and (3.10) are solved using the finite volume method using the one-dimensional wall-model mesh.

e. The obtained wall-stress τ_w is provided to the CFD cell at $(x_{\mathrm{c}},\ y_{\mathrm{c}},\ z_{\mathrm{c}})$, which includes the cut-plane by the object.

3.3 Flow Around a Triangular Column

The flow around a triangular column that contains only sharp-edge separation and hardly depends on the Reynolds number is calculated. The results of the wall-modeled Navier–Stokes simulation is compared using a experiment and an inviscid simulation by the Euler equation.

3.3.1 Simulation Conditions

The flow condition is shown in Table 3.1. The stream-wise length of the triangular column is 37.5mm and the length of the one side D of the triangular column is $25\sqrt{3} \simeq 43.3$mm. The grid system consists of a uniform grid domain and a non-uniform grid domain in the xy direction. The range of the uniform grid domain that consists of cubic cells with constant grid width Δx is $-0.2\text{m} \leq x \leq 0.2\text{m}$, $-0.2\text{m} \leq y \leq 0.2\text{m}$, and $0\text{m} \leq z \leq 0.16\text{m}$. Outside the uniform grid domain, the width of the cuboid cells stretches by 10% between neighbors in the x and y directions. Inflow and outflow boundary condition is decided by Riemann invariants [49]. Boundary values at $y_{\min}$ and $y_{\max}$ are fixed to the free-stream condition. The grid system in the z-direction consists of only a uniform grid, and the periodic boundary condition is applied.

3.3.2 Simulation Results

Isosurfaces of the second invariant of the velocity gradient tensor (Q-criterion) of the fine grid simulations are shown in Figure 3.2. The left figure shows the result of the Euler simulation and the right figure shows the wall-modeled Navier–Stokes simulation. In both figures, flow separation occurs at the downstream-side sharp edges, and a complex vortex structure that contains longitudinal vortices is formed in the wake. The outline of the flow structure by the wall-modelled Navier–Stokes simulation is the same as that of the

Table 3.1: Simulation conditions for the flow around a triangular column.

Ma	Re (Wall-Modeled NS)	$\Delta x/D$
0.3	2.9×10^5	0.092, 0.046

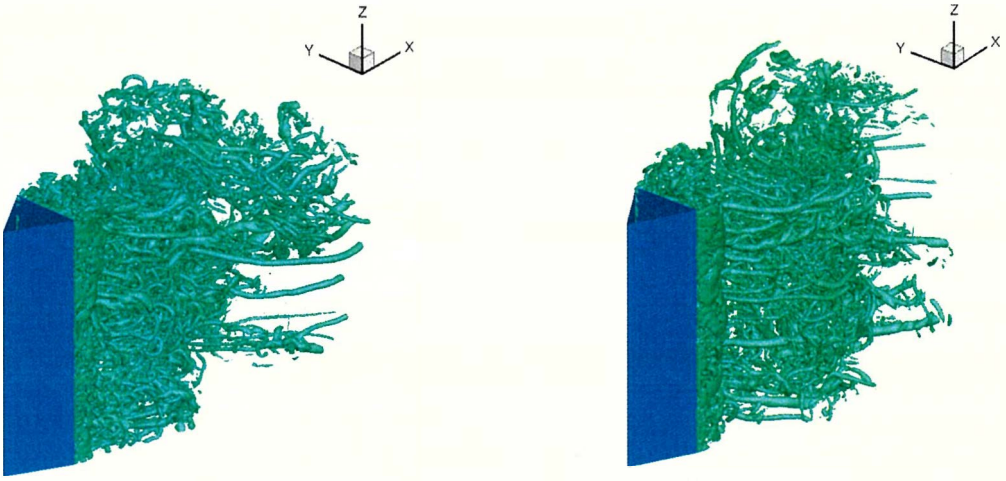

(a) Euler simulation (b) Wall-modelled NS simulation

Fig. 3.2: Isosurfaces of the second invariant of the velocity gradient tensor (Q-criterion).

Euler simulation.

Instantaneous distribution of pressure and velocity in an xy-plane of the fine grid simulation is shown in Figure 3.3. Free shear layers form in the wake of the sharp edges, and the vortices form by the rollup of the free shear layers. Pressure in the wake of the wall-modelled Navier–Stokes simulation is similar to that of the Euler simulation.

Time-averaged distribution of pressure and velocity in an xy-plane of the fine grid simulation is shown in Figure 3.4. The length of the wake of the wall-modelled Navier–Stokes simulation is almost equal to that of the Euler simulation. Pressure distribution in the wake of the wall-modelled Navier–Stokes simulation is slightly different from that of the Euler simulation. However, the surface pressure distributions of the triangular column in both cases do not have noticeable differences. This suggests that the flow field hardly depends on the Reynolds number, and the boundary layer on the triangular column does not play an important role.

The drag coefficient is shown in Table 3.2. The drag coefficient of the fine grid of the Euler simulation is 1.282 and the difference from the experimental value [51] is 3.2%. The difference decreases with grid resolution. The pressure drag coefficients of the fine grid simulation of the wall-modelled Navier–Stokes simulation is 1.284. This value is extremely close to that of the Euler simulation. The difference in the drag coefficient of

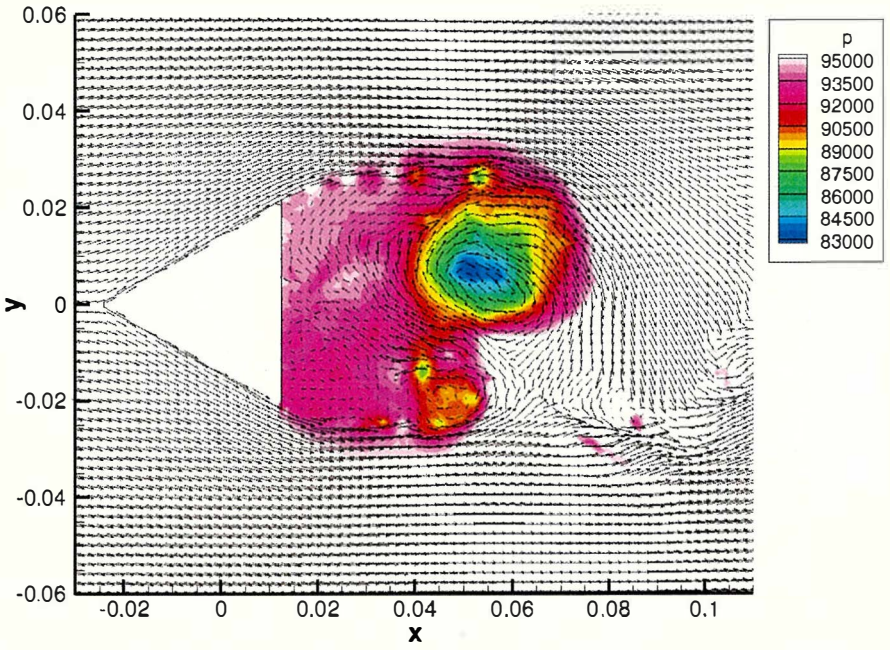

(a) Euler simulation

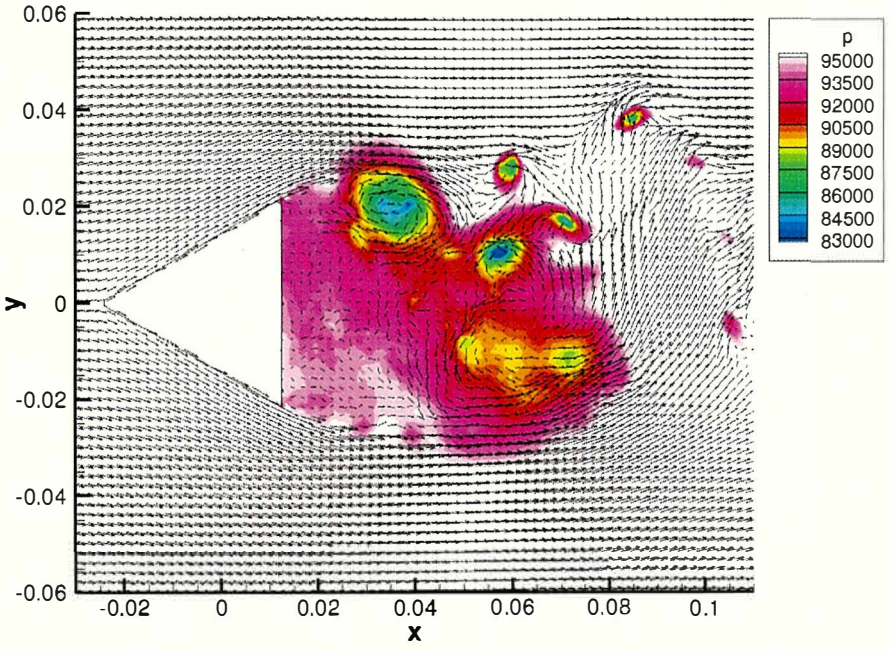

(b) Wall-modelled NS simulation

Fig. 3.3: Pressure contour and velocity vectors at the z = const. plane of the fine grid simulation.

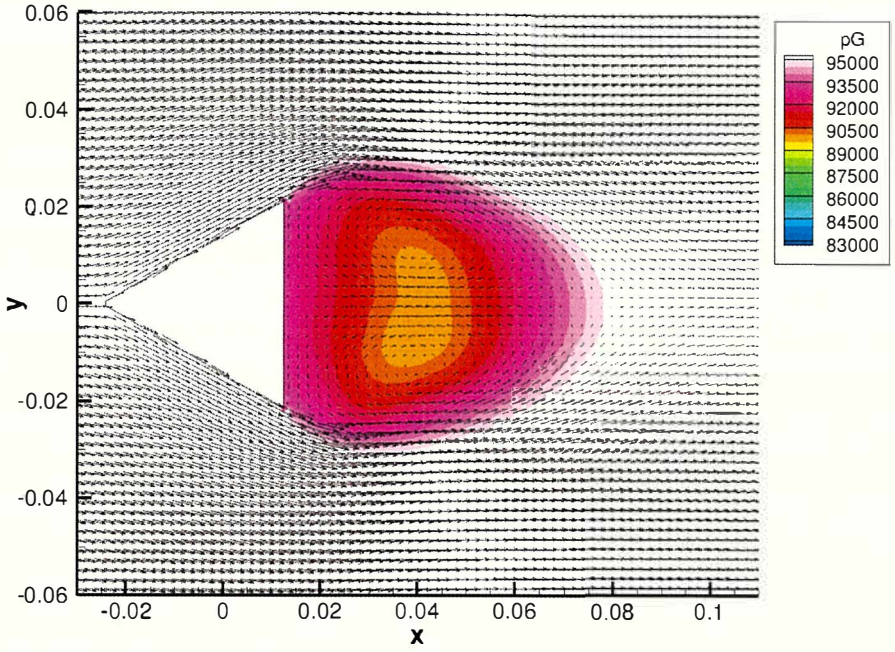

(a) Euler simulation

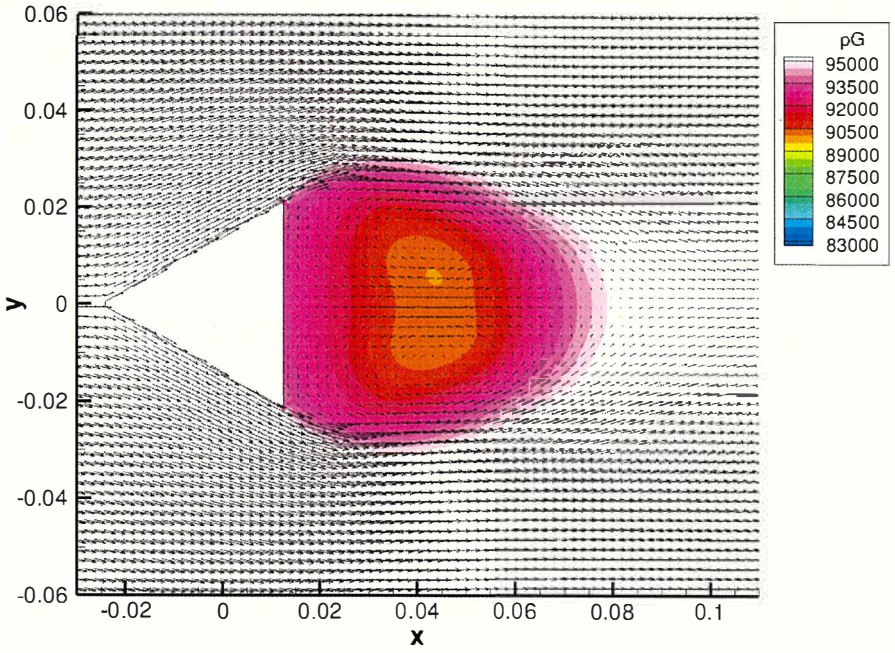

(b) Wall-modelled NS simulation

Fig. 3.4: Time-averaged pressure contour and velocity vectors at the $z = \text{const.}$ plane of the fine grid simulation.

Table 3.2: Drag coefficient and its difference from the experiment (%).

	Coarse	Fine
Euler	1.268 (4.3%)	1.282 (3.2%)
Wall-Modelled NS	1.283 (3.1%)	1.291 (2.6%)
Experiment [51]	1.325	

the wall-modelled Navier–Stokes simulation from the experiment is slightly less than that of the Euler simulation. This improvement is mainly provided by the additional surface friction of the wall-modelled Navier–Stokes simulation. Considering effect of viscosity of the fluid in the wall-modelled Navier–Stokes simulation, this relationship is reasonable.

The computational cost of the wall-modelled Navier–Stokes simulation is 3/2 or more of that of the Euler simulation. Both the wall-modelled Navier–Stokes simulation and the Euler simulation are valid when the separation lines are fixed to the sharp edges of the object. Consequently, it is possible to select one of these simulation methods according to accuracy and computational cost requirements when the separation lines are fixed to the sharp edges and the flow field hardly depends on the Reynolds number.

3.4 Flow Around the 30P30N Three-Element High-Lift Airfoil Configuration

Numerical Euler and wall-modelled Navier–Stokes simulations of the flow around a 30P30N high-lift airfoil configuration were performed. This airfoil is a model of the high-lift device of an aircraft that consists of a slat, main element, and flap. The simulation results were compared with experiments and CFD results using the boundary-fitted mesh method. Based on these comparisons, the prediction capability of the Cartesian cut-cell method with the wall-stress model by Kawai and Larson [18] was discussed.

3.4.1 Simulation Conditions

The flow conditions are provided in Table 3.3. The chord length c of the 30P30N high-lift airfoil configuration is 0.457m following the experiment by Murayama et al. [57]. The grid system consists of a uniform grid domain and a non-uniform grid domain in the xy

Table 3.3: Simulation conditions for the flow around a 30P30N high-lift airfoil configuration.

Ma	Re (Wall-Modeled NS)	α	$\Delta x/c$ Coarse	Medium	Fine
0.17	1.71×10^6	5.5°	2.2×10^{-3}	1.1×10^{-3}	0.55×10^{-3}
		9.5°	2.2×10^{-3}	1.1×10^{-3}	

direction. The range of the uniform grid domain that consists of cubic cells with constant grid width Δx is $-0.1\text{m} \leq x \leq 0.6\text{m}$, $-0.1\text{m} \leq y \leq 0.1\text{m}$, and $0 \leq z \leq 0.052\text{m}$. Outside the uniform grid domain, the width of the cuboid cells stretches by 10% between neighbors in the x and y directions. The boundary condition at the outer edges of the xy-plane is determined by Riemann invariants [49]. The computational grid in xy-plane is shown in Figure 3.5. The grid system in the z direction only consists of a uniform grid, and the

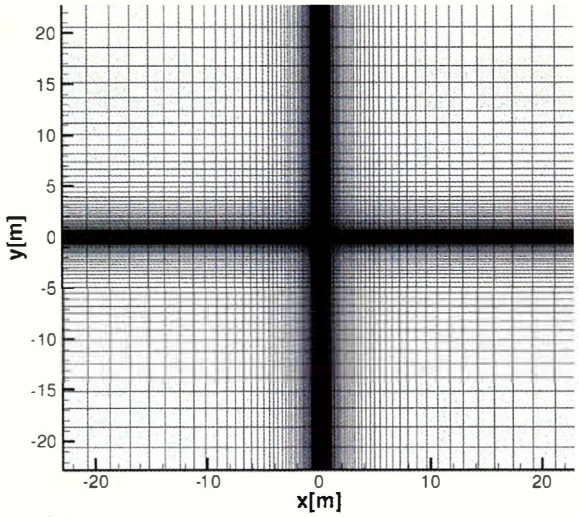

(a) Grid in all the computational domain

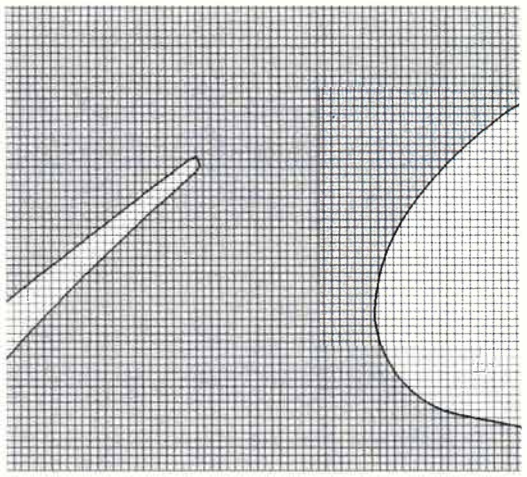

(b) Computational grid around the trailing edge of the slat and the leading edge of the main element

Fig. 3.5: Computational grid around a 30P30N high-lift airfoil configuration.

periodic boundary condition is applied.

3.4.2 Simulation Result by Wall-Modelled Navier–Stokes Simulation

The isosurface of the second invariant of the velocity gradient tensor (Q-criterion) around the 30P30N high-lift airfoil configuration at the angle of attack $\alpha = 5.5°$ is shown in Figure 3.6. Vortices are shed from the trailing edge of the slat (Figure 3.6a), the main element, and the flap. The intermittent vortices of the outer layer of the turbulent boundary layer are generated on the suction side of the main element (Figure 3.6b) and flap.

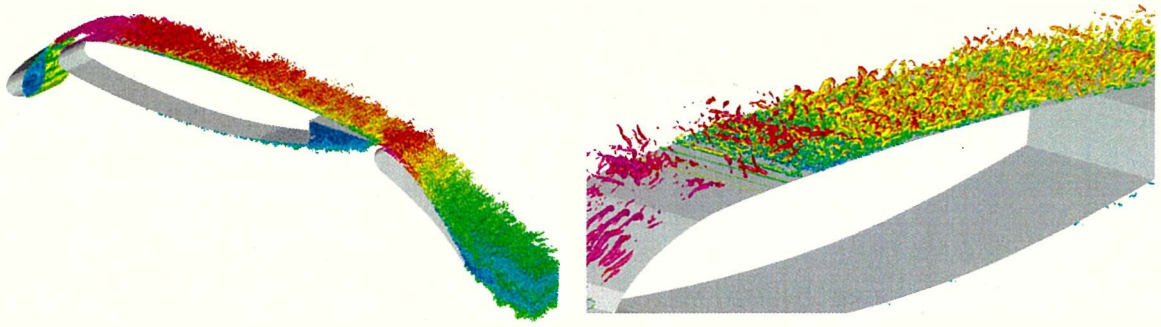

(a) Wake of the slat

(b) Vortices of the outer layer of the turbulent boundary layer on the suction side of the main element

Fig. 3.6: Q-criterion around a 30P30N high-lift airfoil configuration when $\alpha = 5.5°$.

Figure 3.7 shows the distribution of the velocity component u_x at the nearest cell from the airfoil surface and an xy-plane cross-section of the fine grid simulation, providing a close-up view at $x/c \sim 0.15$. The dark blue area in Figure 3.7 shows the negative value of the velocity component, which indicates that the leading-edge separation bubble forms at $x/c \sim 0.15$. The location of the separation bubble is consistent with the experiment [58]. This separation bubble formed in the fine grid simulation but not in the medium and coarse grid simulations.

Figures 3.8a and 3.9 show the instantaneous and time-averaged distribution of the velocity component u_x, respectively, around the flap when $\alpha = 5.5°$. Flow separation occurs on the suction side of the upstream side of the trailing edge of the flap in the instantaneous flow field as shown in Figure 3.8a. It does not reattach before the trailing edge of the flap. In contrast with Figure 3.8a, the flow does not separate in the time-averaged flow field (Figure 3.9). This indicates that the separation near the trailing edge

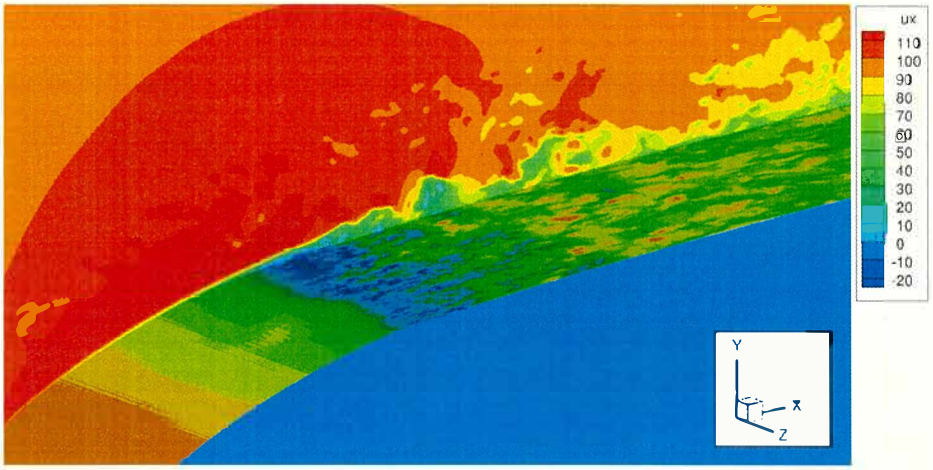

Fig. 3.7: The leading edge separation bubble around $x/c = 0.15$ in the fine grid simulation; color shows velocity component u_x at the nearest cell from the airfoil surface and an x, y cross-section.

Table 3.4: Lift coefficient ($\alpha = 5.5°$) and its difference from the experiment (%); SA DDES, detached eddy simulation with Spalart–Allmaras turbulence model.

		Total Number of Cells	Lift Coefficient
Present Wall-Modelled NS	Coarse	15,972,528	2.60 (7.8%)
	Medium	93,515,136	2.69 (4.6%)
	Fine	612,392,768	2.71 (3.9%)
Boundary-fitted mesh (SA DDES)[59]		70,445,430	2.77 (1.8%)
Hybrid mesh (SA DDES)[60]		242,000,000	2.95 (4.6%)
Experiment [57]			2.82

of the flap occurs intermittently.

The lift coefficients in this study and the α-sweep of that in the experiment in Reference [57] are shown in Figure 3.10. The Cartesian cut-cell simulation with the wall-stress model accurately predicts the lift coefficient.

The lift coefficient of the Cartesian cut-cell simulation with the wall-stress model, the boundary-fitted mesh simulation [59], the hybrid mesh simulation [60], and the experiment [57] are shown in Table 3.4. The hybrid mesh in Reference [60] is composed of the boundary fit mesh in the near-field region and the quadtree-based Cartesian mesh in the far-field region. Compared with the experiment, the Cartesian cut-cell simulation with the wall-stress model underestimates the lift coefficient. The difference from the experiment decreases monotonically with increasing grid resolution. However, the difference decreases

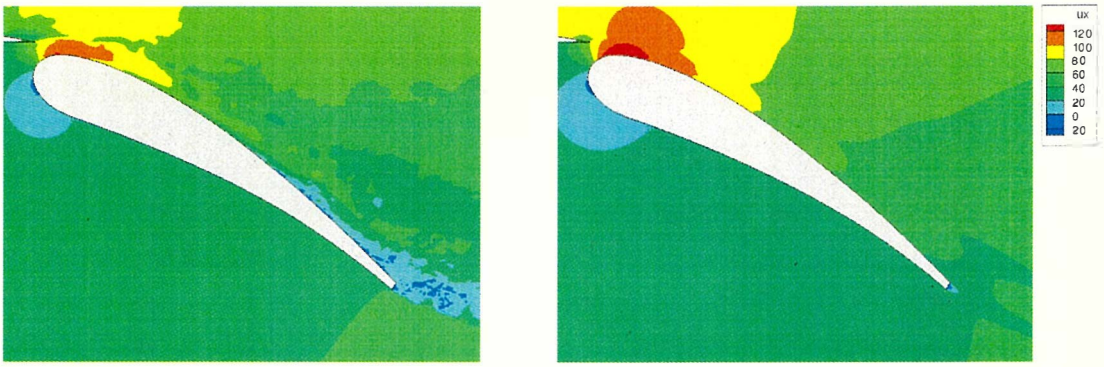

(a) Wall-modelled NS simulation (b) Euler simulation

Fig. 3.8: Instantaneous distribution of velocity component u_x around the flap when $\alpha = 5.5°$.

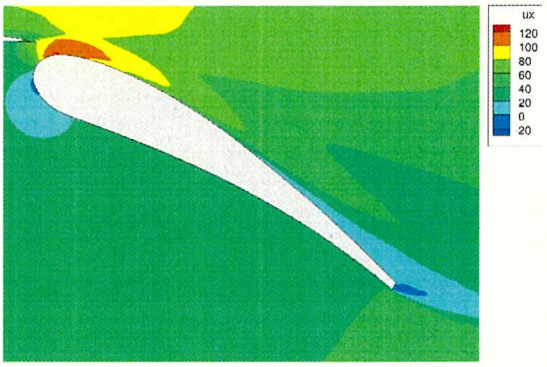

Fig. 3.9: Time-averaged distribution of velocity component u_x by the wall-modelled Navier–Stokes simulation around the flap when $\alpha = 5.5°$.

slower than expected accuracy in the formulation.

The pressure coefficient in the case of $\alpha = 5.5°$ is shown in Figure 3.11. The surface pressure distribution at the pressure side of this study coincides with the experiment and referenced simulations. It indicates that the surface pressure distribution at the pressure side is independent of the grid type and the near-wall treatment.

The Cartesian cut-cell simulation of the present study well estimates the surface pressure distribution as well as the boundary-fitted mesh simulation [59] and hybrid mesh simulation [60], except for the suction side of the slat and the main element suction side of $x/c \leq 0.15$. The curvature of the pressure distribution changes around $x/c = 0.15$, and this x-coordinate coincides with the location from which the vortices of the outer layer of

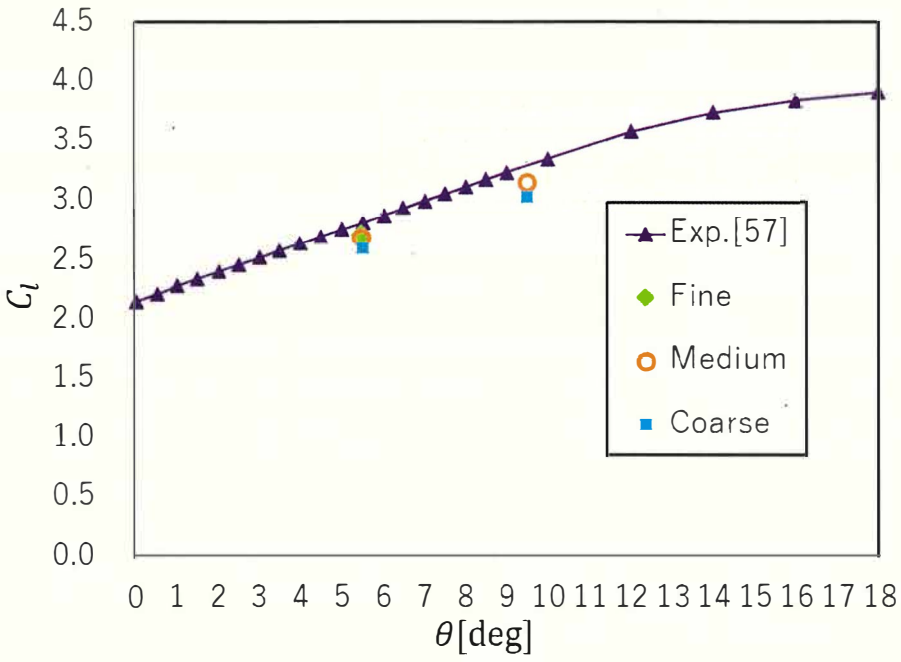

Fig. 3.10: Lift coefficient of the 30P30N high-lift airfoil configuration.

the turbulent boundary layer develop on the suction side of the main element.

The underestimation of the lift coefficient of the present study in Table 3.4 is consistent with the surface pressure distribution in Figure 3.11. The positive error of the surface pressure on the suction side of the main element at $x/c \leq 0.15$ and the suction side of the slat results in the underestimation of the lift. This error is caused by the mismatched estimation of the wall shear stress of the laminar parts of the boundary layers in these areas. The Cartesian cut-cell method experiences difficulty with resolving the laminar boundary layer due to its incompatibility with the grid concentration in the wall-normal direction. This problem is expected to be solved by the future development of the wall-stress model for laminar boundary layers.

The results of the present simulations showed that Cartesian cut-cell simulation with the wall-stress model by Kawai and Larson [18] is one of the most useful schemes for the external flows of $Re \sim 10^6$. The difference in the lift coefficient in the experiment in the medium grid simulation in Table 3.4 is the same as the hybrid mesh simulation [60]. Considering the total number of computational cells, the prediction capability of the

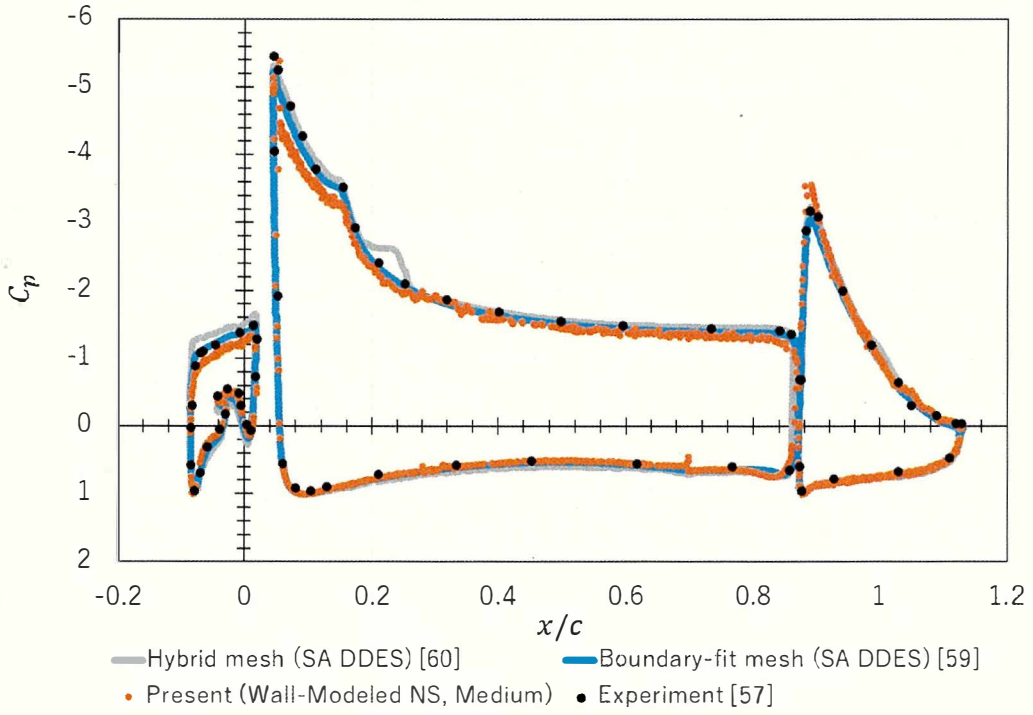

Fig. 3.11: Surface pressure distribution of the 30P30N high-lift airfoil configuration when $\alpha = 5.5°$; SA DDES, detached eddy simulation with Spalart–Allmaras turbulence model.

present Cartesian cut-cell simulation with the wall-stress model is the same as the hybrid simulation [60]. Future improvements in the wall-stress model for the laminar part of boundary layer is expected to produce more accurate prediction within the same degree of accuracy as the boundary-fitted mesh simulation by Sakai [59].

3.4.3 Simulation Result with the Euler Equation

Figure 3.8b shows the instantaneous distribution of the velocity component u_x of the Euler simulation around the flap when $\alpha = 5.5°$. In contrast to the result produced with the wall-modeled Navier–Stokes simulation in Figure 3.8a, flow separation does not occur on the suction side of the flap in Figure 3.8b. This suggests that the Euler simulation does not properly reproduce the flow separation from a smooth surface.

The lift coefficient of the Euler simulation in the medium grid at $\alpha = 5.5°$ is 3.25 and the difference from the experimental result is 13.2%. The Euler simulation overestimates the lift coefficient, and the difference in the lift coefficient in the edium grid of the Euler simulation is obviously larger than that of the coarse grid of the wall-modelled Navier–

Stokes simulation. The Euler simulation is valid only if separation lines are fixed at the sharp edges of the body as shown in Figure 3.2a.

3.5 Conclusions

The prediction capability of the Cartesian cut-cell method with a wall-stress model was discussed in this paper.

In the numerical analysis of the flow around a triangular column, the wall-modelled Navier–Stokes simulation adequately predicted the drag coefficient. In this case of sharp-edge separation flow, the drag coefficients of both the wall-modelled Navier–Stokes simulation and the Euler simulation agreed with the experimental value within a small error. The value of the drag coefficient of the wall-modelled Navier–Stokes simulation was closer to the experimental value compared to that of the Euler simulation.

The difference of the lift coefficient between the Cartesian cut-cell simulation and the experiment monotonically decreases with increasing grid resolution, in the numerical analysis of the flow around the 30P30N three-element high-lift airfoil configuration. The intermittent vortex structure of the outer layer of the turbulent boundary layer was observed on the suction side of the main element and the flap. The intermittent flow separation from the suction side of the airfoil surface of the flap was predicted.

The prediction result of the flows at $Re \sim 10^6$ by the Cartesian cut-cell method with the wall-stress model were equivalent to that by the boundary-fitted mesh methods, except for the laminar parts of the boundary layers. The Cartesian cut-cell method with the wall-stress model is one of the useful methods for high-Reynolds-number flows at $Re \sim 10^6$.

Chapter 4

Coupled Numerical Analysis of Three-Dimensional Unsteady Flow with Pitching Motion of Reentry Capsule

4.1 Introduction

Dynamic instability is one of the unsettled problems in reentry of the blunt-body capsule[23]. The transonic instability may possibly cause the failure to open the parachute in the worst case. Dynamically stable reentry during transonic condition before parachute opening is essential to safety landing. Furthermore, stable parachute opening at low altitude in subsonic condition improves accuracy of landing point owing to reduction of the surface wind effect.

Free-rotation test is a typical experiment using a wind tunnel. Hiraki[24, 25] and Abe *et al.*[26] conducted One degree-of-freedom (1-DoF) free-rotation tests using the same capsule shape using different supporting systems, respectively. These experiments reveals that the phase delay between the pitch angle and aftbody surface pressure fluctuation causes dynamically unstable moment around zero pitch angle.

The Lissajous figure of the pressure difference between two measurement points on the aftbody surface and pitch angle has two knots in Hiraki's experiment[25]. The pressure difference is related to the pitching moment. Considering the contribution of the

base pressure fluctuation to the dynamically unstable moment, it means that the third harmonics have a non-negligible effect on the pitching moment. In order to deepen the discussion of the third harmonics of the pitching moment, it needs to obtain the time history of the pitching moment precisely. Coupled numerical analysis is suitable for this object.

A model equation for the aerodynamic force based on the van der Pol equation was proposed by Hiraki.[24, 25] Abe *et al.*[26] and Kazemba *et al.*[61, 23] proposed model equations introducing phase delay effect called "temporal delay" and "lag time factor," respectively. Abe's model is one of the extensions of Hiraki's model. These model equations well reproduce most of pitch angle oscillations in experiments. However, the third harmonics of the pitching moment did not discussed sufficiently in these researches. Further discussion of the third harmonics of the pitching moment, which plays important role in limit-cycle oscillation, is necessary.

In the present study, large-scaled numerical analysis of the three-dimensional unsteady flow coupled with 1-DoF pitching motion of a reentry capsule is performed. Based on the coupled analysis, the pitching moment coefficient is decomposed into Fourier series, and appropriate modeling of the third harmonics is discussed. Furthermore, a model equation properly considering the third harmonics of the unsteady aerodynamic force is developed.

4.2 Governing equation and simulation method for CFD

In the present study, Cartesian cut-cell method[62] on the Cartesian grid is used for computational fluid dynamics (CFD) analysis. The governing equation is compressible Euler equation. Conservation laws considering Cartesian cut-cell method can be written in the following form.

$$\frac{\partial H\boldsymbol{Q}}{\partial t}+\frac{\partial H\boldsymbol{E}}{\partial x}+\frac{\partial H\boldsymbol{F}}{\partial y}+\frac{\partial H\boldsymbol{G}}{\partial z}=(\boldsymbol{n}\cdot\nabla H)\,\boldsymbol{\sigma}. \tag{4.1}$$

Here, H is the Heaviside function:

$$H(x,y,z)=\frac{1}{2}\{1+\mathrm{sgn}(\phi)\}=\begin{cases}1 & \text{in the air,}\\ 0 & \text{in the capsule.}\end{cases} \tag{4.2}$$

The Heaviside function is determined easily from the level set function:

$$\begin{array}{ll} \phi(x,y,z) > 0 & \text{in the air,} \\ \phi(x,y,z) = 0 & \text{on the capsule surface,} \\ \phi(x,y,z) < 0 & \text{in the capsule.} \end{array} \tag{4.3}$$

$$|\nabla \phi| = 1. \tag{4.4}$$

Since the definition of ϕ is the same as that of the distance function in the level set method [4], this function is called the "level set function," though level set method is not used in the present study but as piecewise-defined elementary functions. The scalar product $\boldsymbol{n} \cdot \nabla H$ is the Dirac delta function, which is defined in the direction normal to the surface of the capsule.

In Eq. (4.1), Heaviside functions in the time differentiation term and the divergence terms are substituted by volume fraction of the cell and area fractions of the cell interface in each direction, respectively. The volume fraction and area fractions are evaluated by the Cartesian cut-cell method. The cell-merging technique[5] is used at each small-cell which has a small gas volume fraction.

The variable $\boldsymbol{\sigma}$ on the right-hand side of Eq. (4.1) represents the wall flux vector (the interaction between the capsule and the air), which is directed into the air from the capsule:

$$\boldsymbol{\sigma} = \begin{pmatrix} 0 \\ pn_x \\ pn_y \\ pn_z \\ p(u_{\mathrm{w}x} n_x + u_{\mathrm{w}y} n_y + u_{\mathrm{w}z} n_z) \end{pmatrix}. \tag{4.5}$$

Mass and heat transfer does not exist in the problems of the present paper.

The conserved quantities $\boldsymbol{Q}$, and the fluxes $\boldsymbol{E}$, $\boldsymbol{F}$, and $\boldsymbol{G}$ in Eq. (4.1) are defined as follows:

$$\boldsymbol{Q} = \begin{pmatrix} \rho \\ \rho u_x \\ \rho u_y \\ \rho u_z \\ e \end{pmatrix}, \quad \boldsymbol{E} = \begin{pmatrix} \rho u_x \\ \rho u_x^2 + p \\ \rho u_y u_x \\ \rho u_z u_x \\ e u_x + p u_x \end{pmatrix},$$

$$\boldsymbol{F} = \begin{pmatrix} \rho u_y \\ \rho u_x u_y \\ \rho u_y^2 + p \\ \rho u_z u_y \\ e u_y + p u_y \end{pmatrix}, \quad \boldsymbol{G} = \begin{pmatrix} \rho u_z \\ \rho u_x u_z \\ \rho u_y u_z \\ \rho u_z^2 + p \\ e u_z + p u_z \end{pmatrix}. \tag{4.6}$$

Conservation equation (4.1) is discretized by cell-centered finite volume method. The advection flux of the compressible Euler equation at the cell interface is calculated using the SLAU method[43]. Velocity components on the cell interface is interpolated by the sixth-order accuracy Weighted Essentially Non-Oscillatory (WENO) scheme[63]. The velocity components are obtained using the modification proposed by Thornber *et al*[46]. The other primitive variables (ρ, p) on the cell interface is incorporated by the fifth-order Monotone Upwind Scheme for Conservation Lows (MUSCL)[56]. Also, the time integration to second-order accuracy is calculated using the TVD Runge-Kutta method[47]. On the coupled analysis, equation of angular motion is calculated using fourth-order Adams-Bashforth method.

4.3 Numerical analysis of the flow around capsule model with fixed pitch angle

CFD simulations of the flow around a capsule model D45S which has spherical base is performed for validation of our simulation code. Pitch angle of the D45S model is fixed. Experimental data of the wind tunnel testing with fixed pitch angle measurements of the D45S spherical-based model and pitching oscillation experiments of D45 frustoconical-based model has been published in Hiraki's study[25]. On the other hand, data of fixed angle measurements of the D45 model is not open to the public. Therefore, we discuss the fixed angle problem of D45S in this section. In the Hiraki's study, dynamic characteristics of the D45 and the D45S model is similar at $M > 1$. Unsteady numerical simulation of the flow around D45S model is sufficient for the validation of the simulation code to reproduce the dynamical characteristics of the D45 model. Schematic of the D45S scale model is shown in Fig. 4.1. Simulation conditions are shown in Table 4.1; the conditions are decided by referring Hiraki's experiments.[25] Grid width Δx is applied on the uniform grid domain, and the width of the domain is $-0.12\text{m} \leq x \leq 0.36\text{m}$, $-0.12\text{m} \leq y \leq 0.12\text{m}$, and $-0.12\text{m} \leq z \leq 0.12\text{m}$. Outside of the uniform grid domain, grid width ratio between neighbor computational cells is 10%.

Flow separation at the shoulder and the fine vortex structures in the wake are observed as shown in Fig. 4.2. Isosurfaces of the second invariant of the velocity gradient tensor are

Table 4.1: Simulation conditions for the flow around D45S model.

α	Ma	$\frac{1}{2}\rho u^2$ [kPa]	$\Delta x/D$
$0° \sim 15°$	1.1	58.9	0.0185, 0.00923
$20° \sim 30°$		70.6	

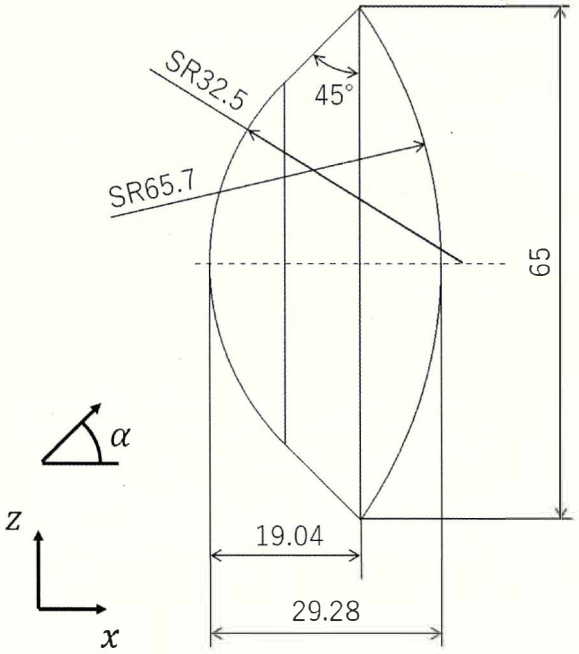

Fig. 4.1: Schematic of D45S scale model.

generated not at the vicinity of the shoulder but at a certain distance from the shoulder. The pressure rises around the stagnation point at the nose and it gradually drops to the shoulder when the pitch angle $\alpha = 0°$.

The typical flow structure in supersonic flows, which includes bow shock, expansion wave on the shoulder and recompression shock in the wake, is observed in Figs. 4.3a and 4.3b. Standing shock wave is formed on the forebody of the D45S in case of $\alpha = 30°$.

Aerodynamic coefficients are obtained by time-averaged values of the unsteady simulation. The sampling of the time-averaged value is started after initial disturbance converges. The sampling time is 0.16s which is 100 times larger than D/u. Drag coefficient, lift coefficient, and pitching moment coefficient shown in Figs. 4.4–4.6 fairly agree

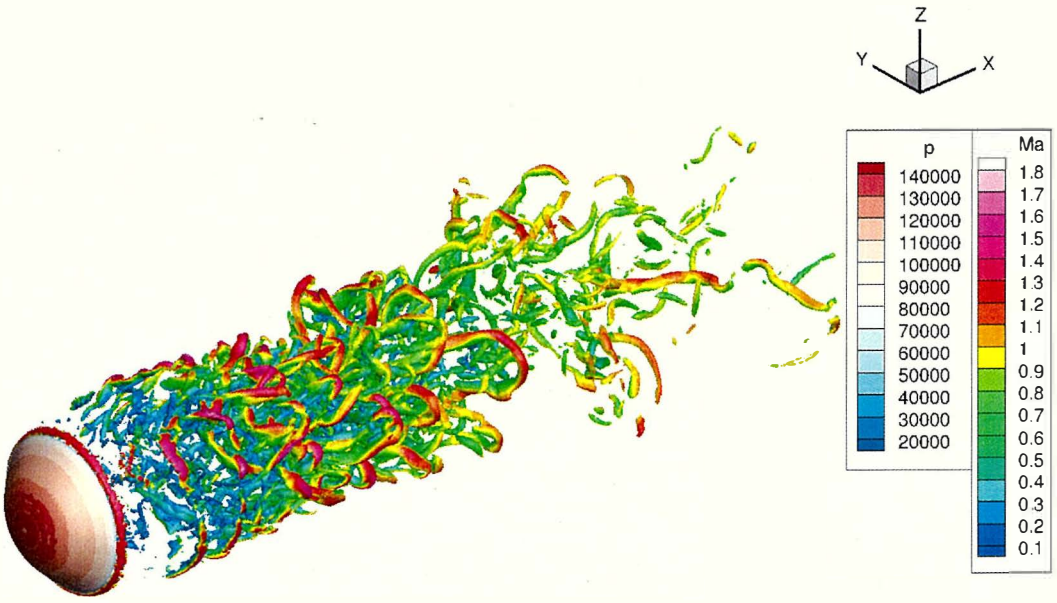

Fig. 4.2: Isosurfaces of the second invariant of the velocity gradient tensor around the D45S model ($\alpha = 0°$).

with Hiraki's experiments[25]. On the fine-grid simulations, the drag coefficient and the lift coefficient are closed to the experimental value with decreasing grid width. The moment coefficient of the fine-grid simulation is in good agreement with the experimental value which has undulation. The aerodynamic coefficients of the coarse-grid simulation well follow the pitch angle dependency of the experimental results. Consequently, the coarse-grid simulation is also acceptable enough for the fixed CFD.

4.4 Coupled CFD analysis with pitching rotation of the capsule

Coupled CFD analysis with 1-DoF pitching rotation of the capsule is performed. Figure 4.7 shows'D45 model, which is a scale model of Hayabusa reentry capsule in 2010.[64] This frustoconical-based model is used in the coupled CFD analysis. The pitching rotation axis parallel to y-axis is placed at 50% position of the total length of the center axis, the pitching moment of inertia is 6.07×10^{-4}. The upstream Mach number is 1.3, and the ratio of grid width to shoulder diameter $\Delta x/D$ is 0.02 (Coarse) and 0.01 (Fine). Grid width Δx

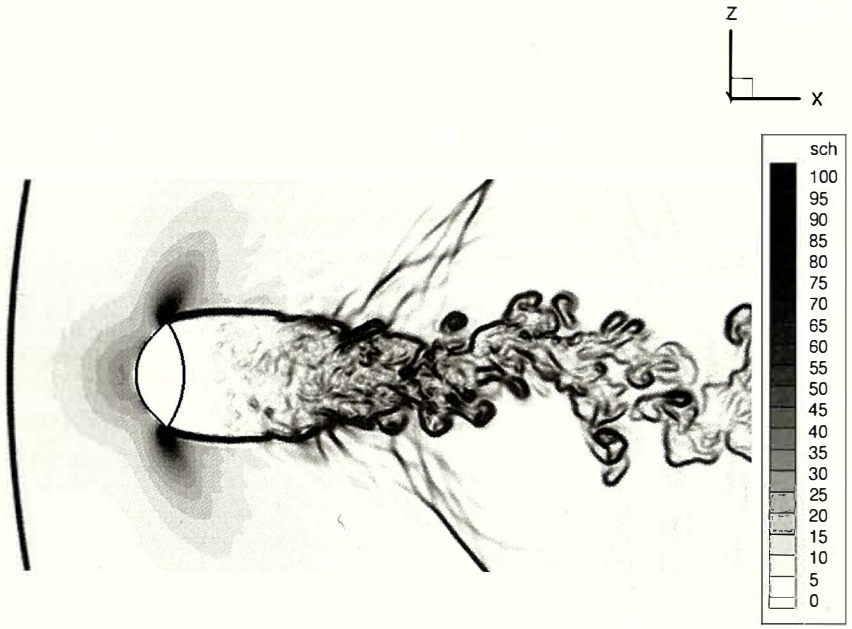

(a) $\alpha = 0°$

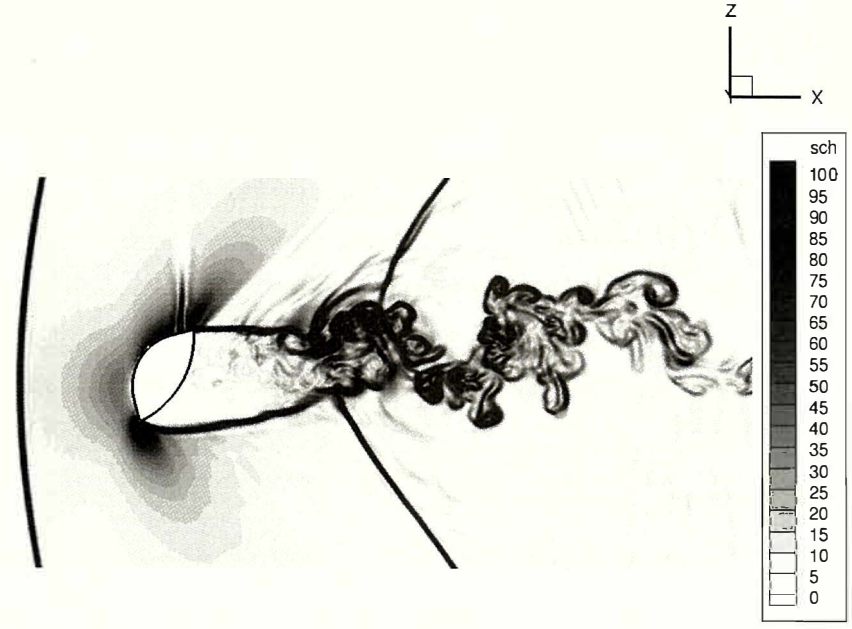

(b) $\alpha = 30°$

Fig. 4.3: Pseudo Schlieren image by the density gradient of the fixed pitch-angle simulation.

is applied on the uniform grid domain $-0.10\text{m} \leq x \leq 0.41\text{m}$, $-0.125\text{m} \leq y \leq 0.125\text{m}$, and $-0.125\text{m} \leq z \leq 0.125\text{m}$. Outside of the uniform grid domain, grid width ratio between

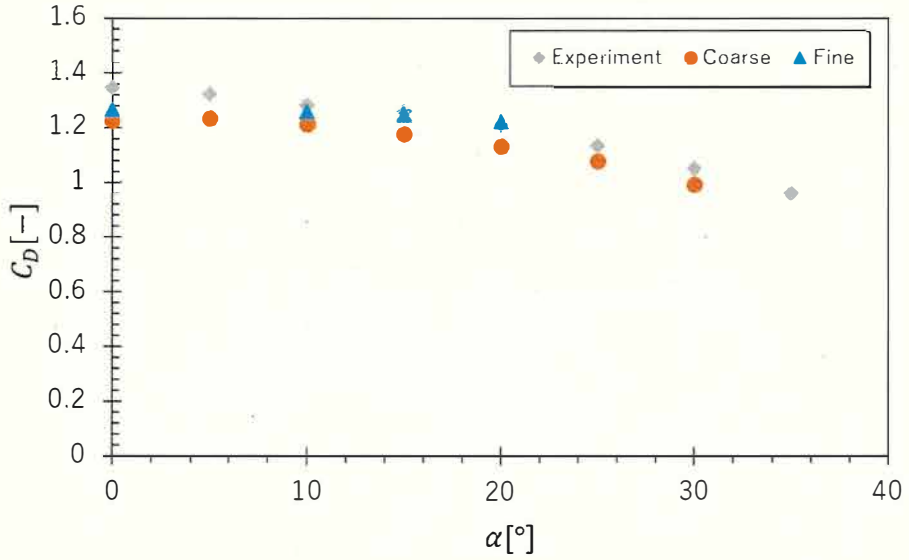

Fig. 4.4: Drag coefficient. Gray square plots show the experimental values and orange circle plots (Coarse) and blue triangle plots (Fine) show the CFD results.

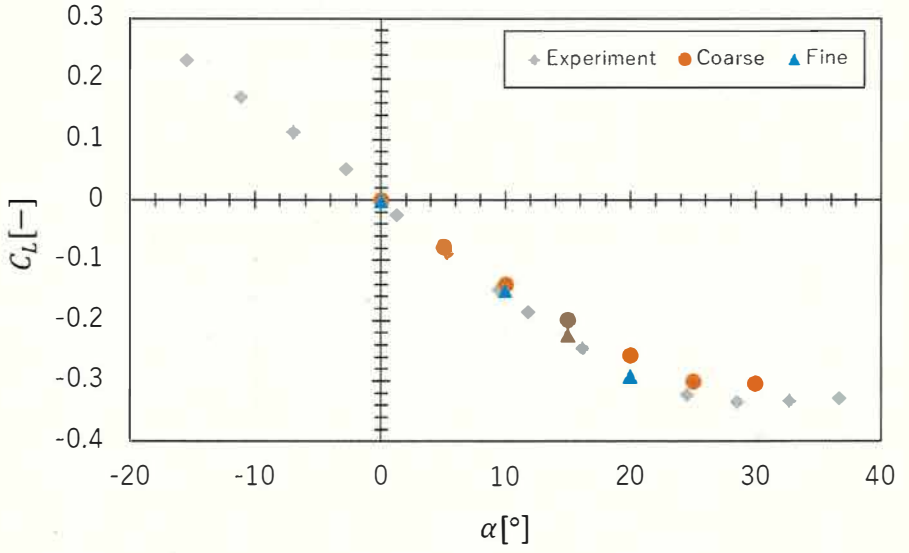

Fig. 4.5: Lift coefficient. Gray square plots show the experimental values and orange circle plots (Coarse) and blue triangle plots (Fine) show the CFD results.

neighbor computational cells is 10%. Initial condition for the coupled CFD analysis is made by fixed CFD analysis using the D45 model at $\alpha = 0$. Furthermore, the initial disturbance of the pitching oscillation is not added.

Results of the 1-DoF coupled CFD analysis are compared with the wind tunnel experiment by Hiraki[24, 25] as shown in Fig. 4.8. Note that the amplitude of the experimental

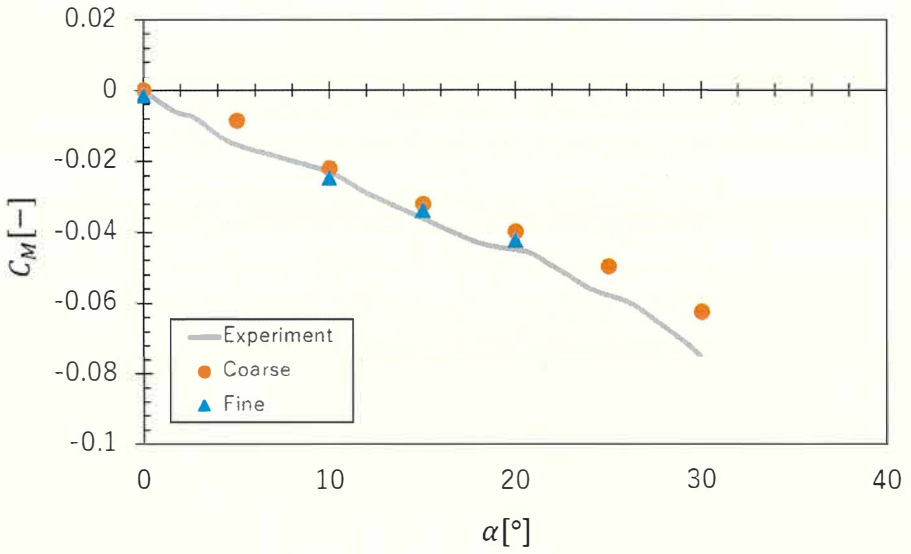

Fig. 4.6: Pitching moment coefficient. Gray line show the experimental value and orange circle plots (Coarse) and blue triangle plots (Fine) show the CFD results.

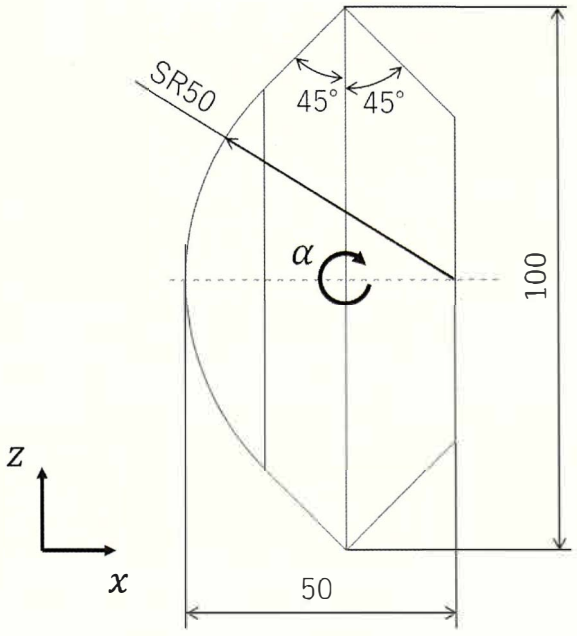

Fig. 4.7: Schematic of D45 model.

result continuously grows up to 20°, though Fig. 4.8 omits the plots to ensure visibility. Self-excitation of pitching oscillation occurs as well as the experiment. Subsequently, limit-cycle oscillation occurs in the fine-grid simulation. The amplitude fluctuations are found as like as that in the experiment during the limit-cycle oscillation. Oscillation frequency is obtained by the elapsed times of the four periods of the limit-cycle oscillation

of the coupled CFD analysis and eight periods of the limit-cycle oscillation of the experiment. The limit-cycle frequency of the coupled CFD analysis is 17.75Hz and that of the experiment is 17.98Hz. The limit-cycle frequency of the coupled CFD analysis well-agrees with the experiment. However, the amplitude is almost a half value of that in the experiment. This underestimate is more remarkable in the coarse-grid simulation, which has much lower amplitude than the experimental result.

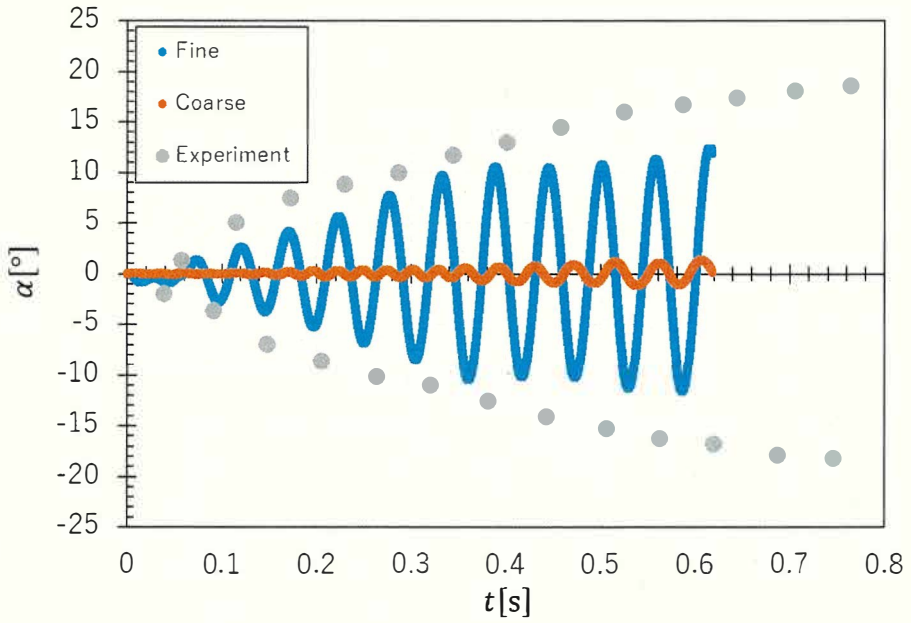

Fig. 4.8: Time history of the pitch angle in 1-DoF coupled CFD analysis. Gray plots are the local maximum and the local minimum values in each cycle which is picked up from the time history of the 1-DoF free oscillation in wind tunnel experiment by Hiraki. Orange and blue lines show the results of the coarse-grid simulation and fine-grid simulation, respectively.

The result of the fine-grid simulation qualitatively agrees with the experiment. The time history of the pitch angle and the pitching moment are obtained. It is judged that the data is sufficient to deepen the understanding of the growing oscillation and the limit-cycle oscillation. However, the reason for the quantitative disagreement of the limit-cycle amplitude is still unclear.

Figure 4.9 shows the phase average of the flow field at $\alpha = 0°$ in pitch-up situation $\dot{\alpha} > 0$. The stagnation point in the wake is the vicinity of the axis of the capsule in the coarse-grid simulation. In the fine-grid simulation, the stagnation point in the wake is different to the coarse-grid simulation.

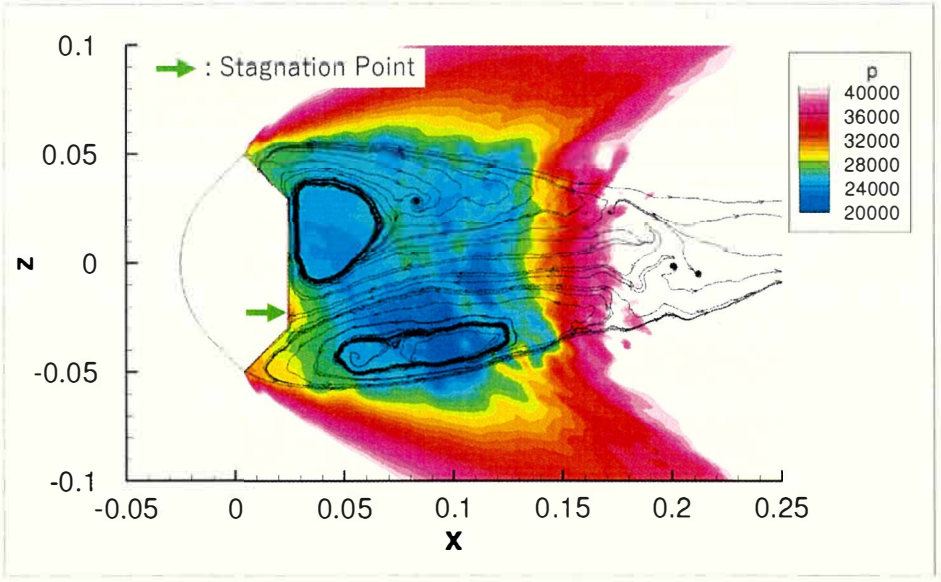

(a) Fine grid

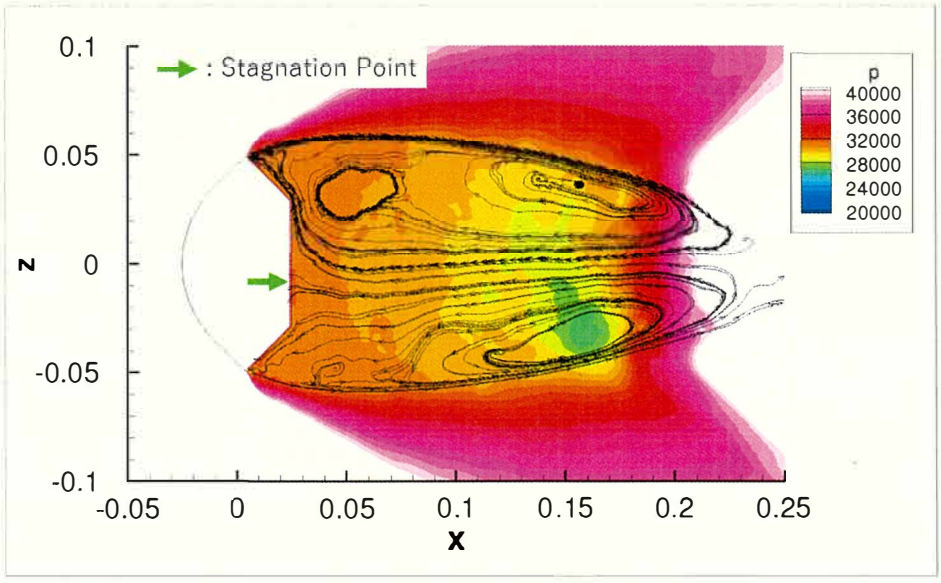

(b) Coarse grid

Fig. 4.9: Streamlines and Pressure distribution of the phase average of the flow field in the symmetric xz plane at $\alpha = 0°$ and $\dot{\alpha} > 0$

Figure 4.10 shows the base pressure distribution of the capsule. Base pressure distribution of the coarse-grid simulation is almost constant. On the other hand, in the fine-gird simulation, base pressure at the upper side is lower than that at the lower side. Consequently, this base pressure distribution causes the unsteady component of pitching moment around $\alpha = 0°$.

Fine vortex structures in the wake in the fine-grid simulation realize the limit-cycle

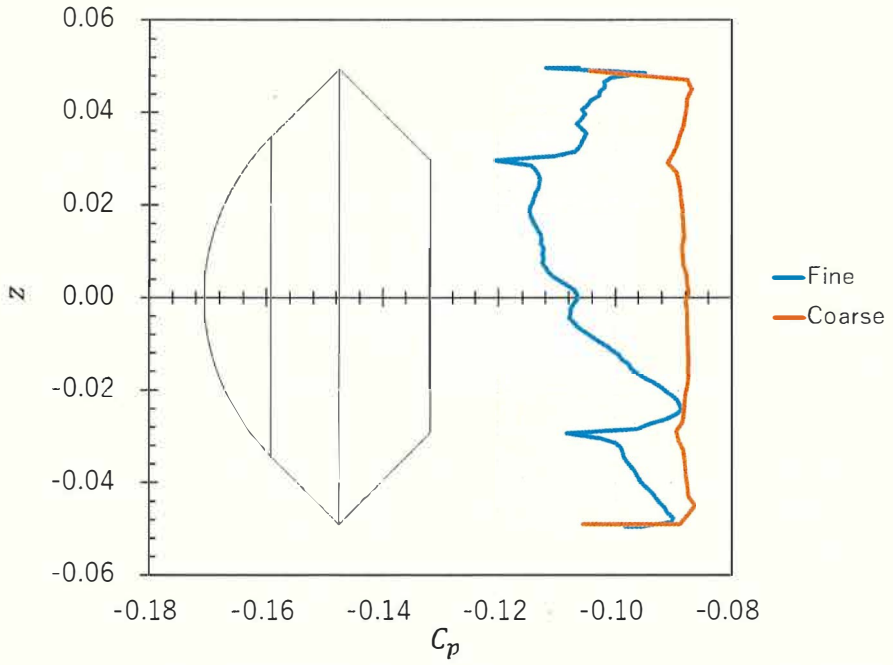

Fig. 4.10: Base pressure distribution of the phase average in the symmetric xz plane at $\alpha = 0°$ and $\dot{\alpha} > 0$.

oscillation in the same order amplitude with the experiment, while self excitation of oscillation is very weak in coarse-grid simulation. It suggests the coupled CFD analysis with the capsule oscillation requires finer grid than that for the CFD analysis around a fixed-angle capsule.

4.5 Fourier Analysis of Limit-Cycle Oscillation

The pitching moment during limit-cycle oscillation is decomposed into Fourier series as follows:

$$M = M_0 C_M, \qquad M_0 = \frac{1}{2}\rho u^2 S D, \tag{4.7}$$

$$\begin{aligned} C_M =& a_1 \cos 2\pi f_{\lim}(t - t_1) + b_1 \sin 2\pi f_{\lim}(t - t_1) \\ &+ a_3 \cos 6\pi f_{\lim}(t - t_1) + b_3 \sin 6\pi f_{\lim}(t - t_1) + \cdots . \end{aligned} \tag{4.8}$$

The constant $t_1 = 0.3185$ is a reference time when $\alpha = 0$ and $\dot{\alpha} > 0$. Figure 4.11 shows the fundamental components, the third harmonics and sum of the higher harmonics. The sine component of the fundamental frequency is major part of the pitching moment. The cosine

and sine components of the third harmonics are stronger than the cosine component of the fundamental frequency. Investigation of the third harmonics are necessary to elucidate the limit-cycle oscillation.

Integral of the angular momentum equation $I\ddot{\alpha} = M$ gives angular velocity:

$$\dot{\alpha} = \frac{M_0}{2\pi f_{\lim} I}\Big\{a_1 \sin 2\pi f_{\lim}(t-t_1) - b_1 \cos 2\pi f_{\lim}(t-t_1) + \frac{a_3}{3}\sin 6\pi f_{\lim}(t-t_1) - \frac{b_3}{3}\cos 6\pi f_{\lim}(t-t_1) + \cdots\Big\}, \tag{4.9}$$

where I denotes moment of inertia of the capsule. Further, integral of $\dot{\alpha}$ gives

$$\alpha = \frac{M_0}{(2\pi f_{\lim})^2 I}\Big\{-a_1 \cos 2\pi f_{\lim}(t-t_1) - b_1 \sin 2\pi f_{\lim}(t-t_1) - \frac{a_3}{9}\cos 6\pi f_{\lim}(t-t_1) - \frac{b_3}{9}\sin 6\pi f_{\lim}(t-t_1) + \cdots\Big\}. \tag{4.10}$$

It is noteworthy that $b_1 < 0$, $|a_1| \ll |b_1|$, $|a_3| \ll |b_1|$, $|b_3| \ll |b_1|$ as shown in Fig. 4.11.

Let us approximate the right-hand side of Eq. (4.8) by using α and $\dot{\alpha}/(2\pi f_{\lim})$. Neglecting small terms of $O(|a_1/b_1|^2)$, $O(|a_3/b_1|^2)$, $O(|b_3/b_1|^2)$ and the higher harmonics, Eq. (4.8) is reduced to

$$C_M = -C_1\,\alpha - \frac{8{C_1}^3 a_3}{9{b_1}^3}\left(\frac{\dot{\alpha}}{2\pi f_{\lim}}\right)\left\{\left(\frac{\dot{\alpha}}{2\pi f_{\lim}}\right)^2 - 3\alpha^2\right\} - \frac{8{C_1}^3 b_3}{9{b_1}^3}\,\alpha\left\{3\left(\frac{\dot{\alpha}}{2\pi f_{\lim}}\right)^2 - \alpha^2\right\}, \tag{4.11}$$

where

$$C_1 = \frac{(2\pi f_{\lim})^2 I}{M_0}. \tag{4.12}$$

4.6 Modeling of the unsteady aerodynamic force

In this section, Eq. (4.11) for limit-cycle oscillation is extended to a model equation for aerodynamic force during growing oscillation as well as limit-cycle oscillation.

The relation $\sin^2 2\pi f_{\lim}(t-t_0) + \cos^2 2\pi f_{\lim}(t-t_0) = 1$ is reduced to

$$\left(\frac{C_1}{b_1}\right)^2\left\{\alpha^2 + \left(\frac{\dot{\alpha}}{2\pi f_{\lim}}\right)^2\right\} = 1 + O\left(\left|\frac{a_3}{b_1}\right|\right) + O\left(\left|\frac{b_3}{b_1}\right|\right) \tag{4.13}$$

when α and $\dot{\alpha}$ are given by Eqs. (4.10) and (4.9), respectively, in limit-cycle oscillation. This relation shows that the amplitude $A_{\lim}$ of α during limit-cycle oscillation is equal to

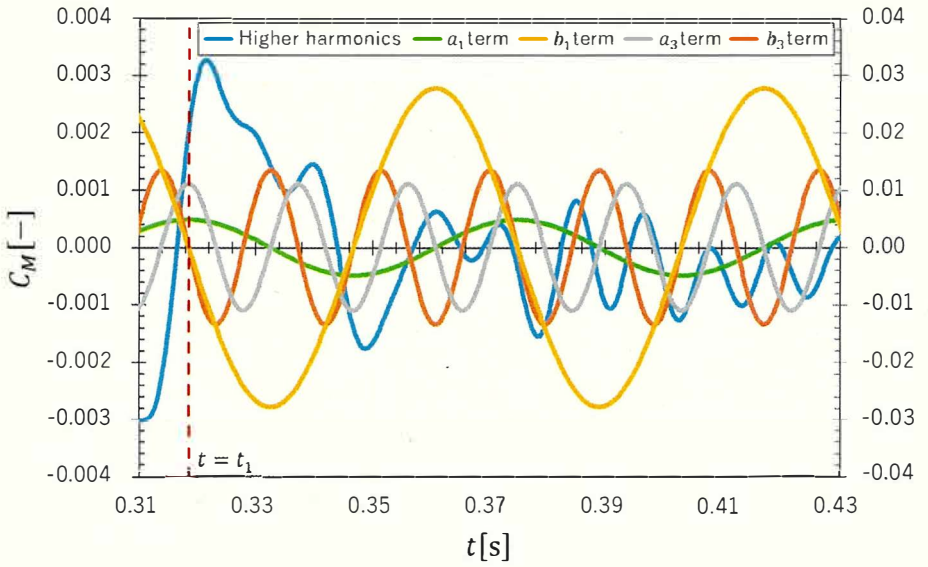

Fig. 4.11: Fourier components of the pitching moment coefficient C_M; the yellow line (b_1 term) is set on the right-hand vertical axis, and other lines (a_1, a_3 and b_3 terms) are set on the left-hand vertical axis.

$-b_1/C_1$. Using this relation, we construct the following model equation for aerodynamic force:

$$\begin{aligned} C_M = -C_1\,\alpha &+ \frac{a_e}{A_{\lim}^3}\left(\frac{\dot{\alpha}}{2\pi f_{\lim}}\right)\left\{A_{\lim}^2 - \alpha^2 - \left(\frac{\dot{\alpha}}{2\pi f_{\lim}}\right)^2\right\} \\ &- \frac{b_e}{A_{\lim}^3}\,\alpha\left\{A_{\lim}^2 - \alpha^2 - \left(\frac{\dot{\alpha}}{2\pi f_{\lim}}\right)^2\right\} \\ &+ \frac{8a_3}{9A_{\lim}^3}\left(\frac{\dot{\alpha}}{2\pi f_{\lim}}\right)\left\{\left(\frac{\dot{\alpha}}{2\pi f_{\lim}}\right)^2 - 3\alpha^2\right\} \\ &+ \frac{8b_3}{9A_{\lim}^3}\,\alpha\left\{3\left(\frac{\dot{\alpha}}{2\pi f_{\lim}}\right)^2 - \alpha^2\right\}, \end{aligned} \tag{4.14}$$

The second and third terms of the right-hand side cause the growing oscillation, meanwhile limit-cycle oscillation does not affected by these terms in any values of the constants a_e and b_e.

Limit-cycle frequency $f_{\lim} = 17.75$Hz is decided by the result of the coupled CFD analysis with the capsule oscillation, and it gives $C_1 = 0.152$. Fourier series expansion decides Fourier coefficients $b_1 = -0.0277$, $a_3 = 0.00110$ and $b_3 = -0.00134$. Fitting parameter b_e reproduces the initial frequency f_0 in the growing oscillation, and is estimated

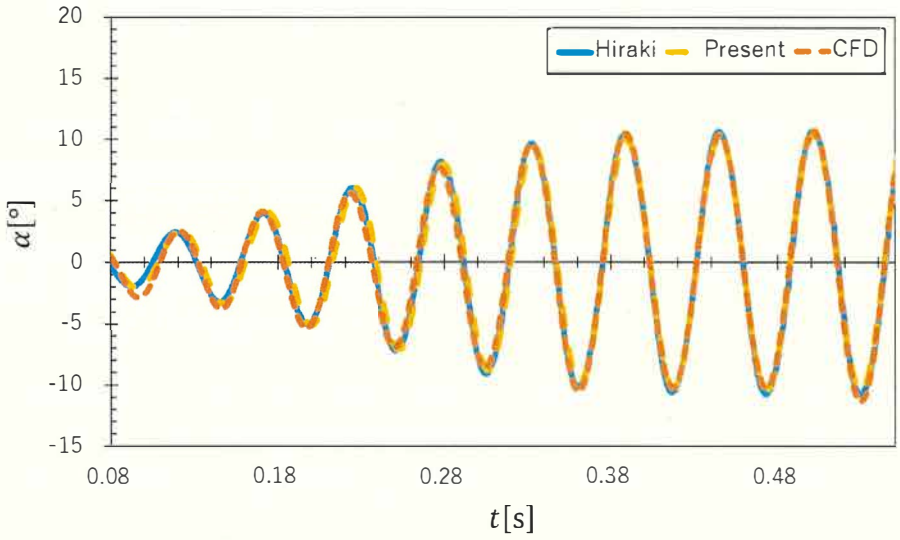

Fig. 4.12: Time history of the pitch angle of the capsule.

as follows:

$$b_e = \left(1 - \frac{f_0^2}{f_{\lim}^2}\right) b_1 = 0.00575 \tag{4.15}$$

where $f_0 = 19.5$Hz is decided by the results of the coupled CFD analysis. Another fitting parameter a_e reproduces the envelope curve of the growing oscillation, and is estimated to be 0.00481.

Hiraki's model[24, 25] of the pitching moment coefficient based on van der Pol equation is in the following form:

$$C_M = a\,\alpha + b\,\alpha^3 + c\,\dot{\alpha}\,\left(A_{\lim}^2 - 4\alpha^2\right). \tag{4.16}$$

Variables a, b and c are fitting parameters. Only if $a_e = 8a_3/9$ and $b_e = -8b_3/3$, Hiaki's model coincides with Eq. (4.14). Nevertheless, $a_e = 8a_3/9$ and $b_e = -8b_3/3$ does not gives good approximation for the growing oscillation. Therefore, lack of the terms $\alpha^2\dot{\alpha}$ and $\dot{\alpha}^3$ in Hiraki's model is remarkable.

Numerical solutions of initial value problem $I\ddot{\alpha} = M_0 C_M$ are obtained by the present model and Hiraki's model. Figure 4.12 shows the time history of the pitch angle α obtained from the coupled CFD analysis, the present model and Hiraki's model. Parameters $a = -0.176$, $b = 0.95$ and $c = 0.007$ are used in Hiraki's model. The numerical solutions of α by both models well reproduce time history of the CFD analysis.

Figure 4.13 shows the time history of the pitching moment coefficient C_M obtained

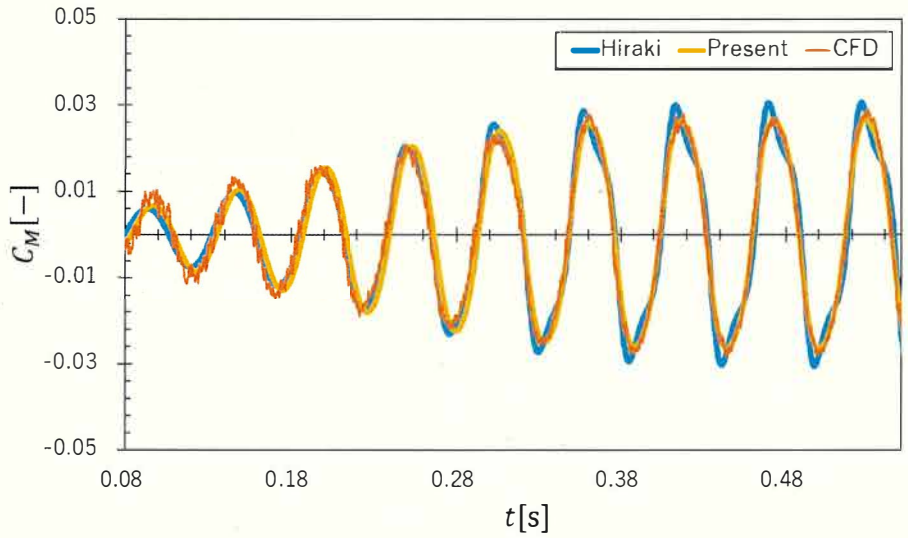

Fig. 4.13: Time history of the pitching moment coefficient.

from the coupled CFD analysis, the present model and Hiraki's model. The numerical solution of C_M by the present model reproduces the time history of the CFD analysis. The numerical solution of C_M by Hiraki's model also reproduces the time history of the CFD analysis during growing oscillation. However, Hiraki's model overestimates the peak value of the limit-cycle oscillation and the waveform is distorted in the range of $|C_M| > 0.02$.

Moment coefficient is decomposed into static component and dynamic component as follows:

$$C_M = C_{M\mathrm{st}} + C_{M\mathrm{dy}}, \qquad C_{M\mathrm{st}} = -C_1\alpha. \tag{4.17}$$

Figure 4.14 shows the work per unit time $\dot{\alpha}C_{M\mathrm{dy}}$ that the dynamic component of the moment does during the limit-cycle oscillation. The asymmetricity of the CFD results is caused by the shortage of the phase-averaged cycles. The asymmetricity is expected to reduce with the increment of the averaged cycles. The present model reproduces the major part of the dynamic work per unit time acting on the capsule during the limit-cycle oscillation. From the aspect of the positive dynamic work per unit time around maximum (or minimum) α, the present model is qualitatively agreed with coupled CFD result. The quantitative disagreement between the CFD result and the present model is caused by ignoring the higher harmonics for simplicity. On the other hand, Hiraki's model overestimates the dynamic work per unit time, and the local maximum phase is appreciably different from CFD result. Also, dynamic work per unit time of the Hiraki's

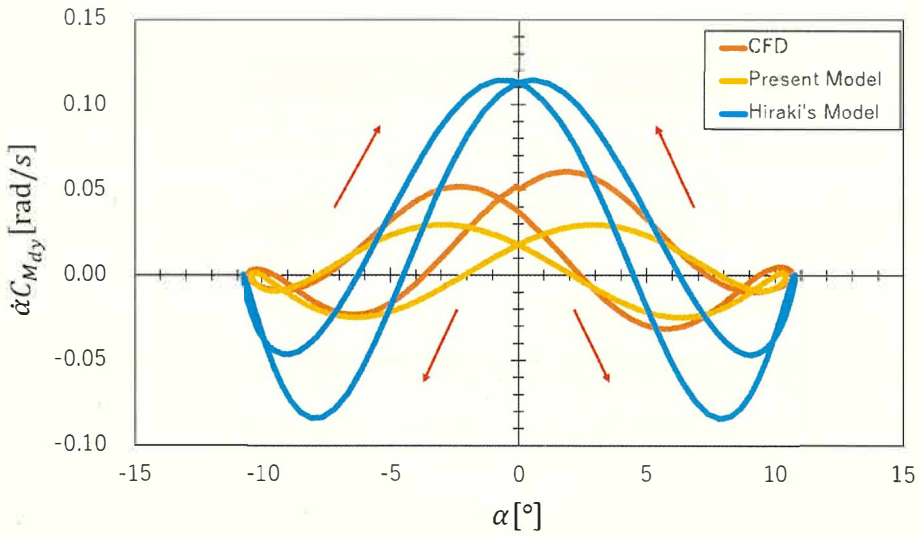

Fig. 4.14: Dynamic component $\dot{\alpha}\, C_{M\mathrm{dy}}$ of the aerodynamic work per unit time acting on the capsule.

model is not positive around maximum (or minimum) α, thus Hiraki's model qualitatively disagreed with $\dot{\alpha}C_{M\mathrm{dy}}$ of the CFD result.

Figure 4.15 shows the dynamic component $C_{M\mathrm{dy}}$ of the moment coefficient of the numerical solution of the present model plotted on the α–$\dot{\alpha}/(2\pi f)$ phase plane. During the growing oscillation, the sign of $C_{M\mathrm{dy}}$ changes in the fundamental frequency, while the sign changes in the third harmonics frequency in the limit-cycle oscillation.

Considering clockwise time-development of the state point in the phase plane, local maximum phase of $C_{M\mathrm{dy}}$ advances from vertical axis. We obtain the dynamic component $C_{M\mathrm{dy}} = C_M + C_1\alpha$ from Eqn. (4.14). In case of limit-cycle, $C_{M\mathrm{dy}}$ is described by using trigonometric function by substituting Eqs. (4.9) and (4.10). Neglecting the small terms, the dynamic component is reduced to $\cos\{3(2\pi f_{\mathrm{lim}}t + \varphi_{\mathrm{lim}})\}$ with a certain coefficient. On the other hand, during initial stage of growing, $C_{M\mathrm{dy}}$ is reduced to $a_e(\dot{\alpha}/2\pi f_{\mathrm{lim}})/A_{\mathrm{lim}} - b_e\alpha/A_{\mathrm{lim}}$. Angular momentum equation using this approximation gives the solution

$$\alpha = q_1 \exp\left(\frac{a_e \pi f_{\mathrm{lim}} t}{A_{\mathrm{lim}} C_1}\right) \sin\left\{2\pi f_{\mathrm{lim}}(t - t_1)\sqrt{1 - \left(\frac{a_e}{2A_{\mathrm{lim}}C_1}\right)^2 + \frac{b_e}{A_{\mathrm{lim}}C_1}}\right\}. \tag{4.18}$$

Substituting this solution into the simplified equation of $C_{M\mathrm{dy}}$ and neglecting small order terms of $\mathcal{O}(a_e/A_{\mathrm{lim}}C_1)$ and $\mathcal{O}(b_e/A_{\mathrm{lim}}C_1)$, we obtain

$$C_{M\mathrm{dy}} = q_1 \frac{\sqrt{a_e^2 + b_e^2}}{A_{\mathrm{lim}}} \exp\left(\frac{a_e \pi f_{\mathrm{lim}} t}{A_{\mathrm{lim}} C_1}\right) \cos\{2\pi f_{\mathrm{lim}}(t - t_1) + \varphi_0\}. \tag{4.19}$$

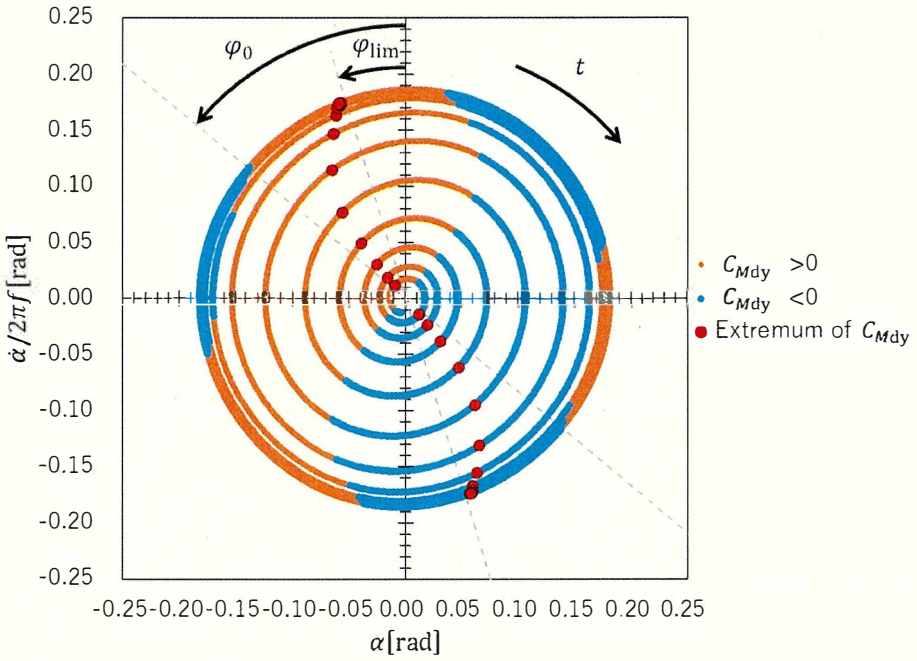

Fig. 4.15: Dynamic component C_{Mdy} of the moment coefficient on the α–$\dot{\alpha}/(2\pi f)$ phase plane.

Initial phase advance φ_0 in the growing oscillation and phase advance $\varphi_{\lim}$ in limit-cycle oscillation are evaluated as follows:

$$\varphi_0 = \tan^{-1}\left(\frac{b_e}{a_e}\right), \qquad \varphi_{\lim} = \frac{1}{3}\tan^{-1}\left(-\frac{b_3}{a_3}\right). \tag{4.20}$$

Phase advance of C_{Mdy} shifts from initial value $\varphi_0 = 50.1°$ to $\varphi_{\lim} = 16.9°$ in limit-cycle oscillation. It is suggested that progress of oscillation growth up to the limit-cycle oscillation is specified by $\varphi_{\lim} \leq \varphi \leq \varphi_0$. Note that the value of the phase advances are not universal but specified with the numerical (experimental) conditions. Phase advance is one of the potential criteria that quantify the dynamic stability of the reentry capsule. It requires to validate it by many experiments and numerical simulations data.

4.7 Conclusions

Coupled CFD analysis with 1-DoF pitching motion of a scale model of a reentry capsule is performed. The following findings are obtained.

Numerical simulations of the flow around D45S capsule with fixed pitch angle is performed before 1-DoF coupled analysis. Aerodynamic coefficients coincides with the

experiment[25].

The coupled CFD analysis with pitching oscillation of D45 capsule using a fine grid reproduces the same frequency and a half amplitude compared with the experimental result by Hiraki.[24, 25] The axis of vortex ring in the wake of the phase average is displaced to the lower side of the capsule base when $\alpha = 0$ and $\dot{\alpha} > 0$, and pressure on the upper side of the capsule base decreases. Consequently, dynamic component of unsteady pitching moment arises.

Pitching moment coefficient is decomposed into Fourier series. The amplitude of the third harmonics is larger than the cosine component of the fundamental frequency.

The model equation for the pitching moment which properly considers the third harmonics is proposed. Numerical solution of α by the present model reproduces almost the same oscillation with the coupled CFD analysis as well as that by Hiraki's model[24, 25]. Moreover, the dynamic component $\dot{\alpha} C_{M\mathrm{dy}}$ of the unsteady aerodynamic work per unit time of the present model gives better estimate than Hiraki's model even though the present model equation does not require increase of the number of fitting parameters. Consequently, the present model equation gives better result than Hiraki's model equation.

Chapter 5

Conclusion

5.1 Summary of the present study

Chapter 2 "Applicability of the Inviscid Simulations to the Flow around a Body with Sharp-Edge Separation using Cartesian Cut-Cell Method"

The applicability of inviscid simulations to real flows is discussed using the Cartesian cut-cell method in this chapter.

Numerical simulations of the flow past a triangular column are performed. For the three-dimensional simulations, even though they are inviscid calculations, the difference between the calculated and reference experimental values of the drag coefficient is less than 1%. The difference also decreases as the grid width is refined, i.e., grid convergence is confirmed. The trailing edges of the triangular column generate two shear layers behind the column. Subsequently, a vortex street is formed in the wake by rolling up of the shear layers. The same flow structure has been observed in experiments [52, 50]. These results indicate that the present inviscid simulation reproduces the main parts of the real phenomena.

The major characteristic frequencies of the lift and the drag fluctuations are calculated using FFT analysis. The characteristic frequency of the lift match the frequency of von Kármán's vortex, as obtained in both the experiments [52, 50] and the LES [50]. Moreover,

the slow fluctuations in the drag match the fluctuations in the width of the wake (i.e., the distance between the two shear layers).

Validations confirm that the three-dimensional inviscid simulations provide valid representations of certain kinds of flows around a body with sharp-edge separation as well as flows without separations. However, two-dimensional inviscid simulations are invalid for the flows that contain flow separation. They predict extremely large pressure drops in the vortices, which do not occur in either the three-dimensional simulations or the experiments.

Chapter 3 "Applicability of the Wall-Modeled Cartesian Cut-Cell Method to the High Reynolds Number Flows"

Application of the WMNS to Cartesian cut-cell method and the applicability of invisid simulation of Euler equation are investigated in this chapter.

Euler simulation and WMNS simulation of the flow around a triangular column is performed. According to experiments, separation line of this flow is fixed to the sharp-edge, and this flow hardly dependents on the Reynolds number. Euler simulation gives the qualitatively the same flowfield as the WMNS simulation. WMNS simulation gives a better estimation of the drag coefficient rather than the Euler simulation, but the difference from the experiment is at most 3.2% in the Euler simulation. This fact suggests the validity of the Euler simulation for the sharp-edge separation flow. Furthermore, the Euler simulation reduces the computational cost to 2/3 or less of WMNS's cost. This advantage is appreciable in lage-scale computation.

Vortices generation in the outer-layer of the TBL in the WMNS simulation of the flow around the 30P30N high-lift airfoil configuration, and intermittently separation occurs around the trailing edge of the flap suction side. The WMNS simulation well estimates the lift coefficient.

In the Euler simulation, separation on the flap suction side of the 30P30N high-lift airfoil configuration does not occur. Further, the Euler simulation overestimates the lift coefficient, and this estimation is not useful. Consequently, the Euler simulation is insufficient for prediction of the flow including the separation from smooth surface.

Chapter 4 "Coupled Numerical Analysis of Three-Dimensional Unsteady Flow with Pitching Motion of Reentry Capsule"

Coupled CFD analysis with 1-DoF pitching motion of a scale model of a reentry capsule is performed. The following findings are obtained in this chapter.

The coupled CFD analysis with pitching oscillation of D45 capsule using a fine grid reproduces the same frequency and a half amplitude compared with the experimental result by Hiraki.[24, 25] The axis of vortex ring in the wake of the phase-lock average is displaced to the lower side of the capsule base when $\alpha = 0$ and $\dot{\alpha} > 0$, and pressure on the upper side of the capsule base decreases. Consequently, dynamic component of unsteady pitching moment arises.

Pitching moment coefficient is decomposed into Fourier series. The amplitude of the third harmonics is larger than the cosine component of the fundamental frequency.

The model equation for the pitching moment which fully includes the third harmonics is proposed. Numerical solution of α by the present model reproduces almost the same oscillation with the coupled CFD analysis as well as that by Hiraki's model[24, 25]. Moreover, the dynamic component $\dot{\alpha}\, C_{M\mathrm{dy}}$ of the unsteady aerodynamic work of the present model gives better estimate than Hiraki's model even though the present model equation does not require increase of the number of fitting parameters. Phase advance of the dynamic component $C_{M\mathrm{dy}}$ of the moment coefficient on the phase plane varies from initial phase advance $\varphi_0 = 50.1°$ up to limit-cycle phase advance $\varphi_{\mathrm{lim}} = 16.9°$.

The present thesis suggests the developability of the Cartesian grid solver to the high Reynolds number flows. Wall-modeled Navier-Stokes simulation is compatible with Cartesian cut-cell method, and also Euler simulation which limited to sharp-edge separated flows gives good estimation as well as WMNS simulation. Cartesian cut-cell method is a useful solver for coupled analysis owing to its low grid generation cost and mass conservation. Cartesian cut-cell method is expected to evolve as a simulation tool for high Reynolds number flows.

References

[1] Vassberg, John and Jameson, Antony"In Pursuit of Grid Convergence, Part I: Two-Dimensional Euler Solutions," in *27th AIAA Appl. Aerodyn. Conf.* (June) , pp. 1–34, Reston, Virigina: American Institute of Aeronautics and Astronautics (2009)

[2] Vinokur, Marcel"Conservation equations of gasdynamics in curvilinear coordinate systems," *J. Comput. Phys.*, **14** (2) , pp. 105–125 (1974) .

[3] Hirt, C.W and Nichols, B.D"Volume of fluid (VOF) method for the dynamics of free boundaries," *J. Comput. Phys.*, **39** (1) , pp. 201–225 (1981) .

[4] Sussman, Mark, Smereka, Peter, and Osher, Stanley"A Level Set Approach for Computing Solutions to Incompressible Two-Phase Flow," *J. Comput. Phys.*, **114** (1) , pp. 146–159 (1994) .

[5] Clarke, D. K., Hassan, H. A., and Salas, M. D."Euler calculations for multielement airfoils using Cartesian grids," *AIAA J.*, **24** (3) , pp. 353–358 (1986) .

[6] Yang, G., Causon, D. M., and Ingram, D. M."Calculation of compressible flows about complex moving geometries using a three-dimensional Cartesian cut cell method," *Int. J. Numer. Methods Fluids*, **33** (8) , pp. 1121–1151 (2000) .

[7] Harada, Motoshi and Imamura, Taro"Comparison of Immersed Boundary Method and Cut-Cell Method on Cartesian Grids – Validation of Pressure and Shear Stress Distributions on Near-Wall Region –," *J. Japan Soc. Aeronaut. Sp. Sci.*, **64** (3) , pp. 200–207 (2016) , (in Japanese).

[8] Peskin, Charles S "Numerical analysis of blood flow in the heart," *J. Comput. Phys.*, **25** (3) , pp. 220–252 (1977) .

[9] Iaccarino, Gianluca and Verzicco, Roberto "Immersed boundary technique for turbulent flow simulations," *Appl. Mech. Rev.*, **56** (3) , p. 331 (2003) .

[10] Mittal, Rajat and Iaccarino, Gianluca "Immersed Boundary Methods," *Annu. Rev. Fluid Mech.*, **37** (1) , pp. 239–261 (2005) .

[11] DeZeeuw, Darren and Powell, Kenneth G. "An Adaptively Refined Cartesian Mesh Solver for the Euler Equations," *J. Comput. Phys.*, **104** (1) , pp. 56–68 (1993) .

[12] Ishida, Takashi, Takahashi, Shun, and Nakahashi, Kazuhiro "Efficient and Robust Cartesian Mesh Generation for Building-Cube Method," *J. Comput. Sci. Technol.*, **2** (4) , pp. 435–446 (2008) .

[13] Choi, Haecheon and Moin, Parviz "Grid-point requirements for large eddy simulation: Chapman's estimates revisited," *Phys. Fluids*, **24** (1) , pp. 1–6 (2012) .

[14] Nikitin, N. V., Nicoud, F., Wasistho, B., Squires, K. D., and Spalart, P. R. "An approach to wall modeling in large-eddy simulations," *Phys. Fluids*, **12** (7) , pp. 1629–1632 (2000) .

[15] Baurle, R. A., Tam, C. J., Edwards, J. R., and Hassan, H. A. "Erratum: Hybrid Simulation Approach for Cavity Flows: Blending, Algorithm, and Boundary Treatment Issues (AIAA Journal (2003) 41:8 (1463-1480))," *AIAA J.*, **41** (10) , p. 2079 (2003) .

[16] Nicoud, F., Baggett, J. S., Moin, P., and Cabot, W. "Large eddy simulation wall-modelling based on suboptimal control theory and linear stochastic estimation," *Phys. Fluids*, **13** (10) , pp. 2968–2984 (2001) .

[17] Bose, S. T. and Moin, P. "A dynamic slip boundary condition for wall-modeled large-eddy simulation," *Phys. Fluids*, **26** (1) (2014) .

[18] Kawai, Soshi and Larsson, Johan"Wall-modeling in large eddy simulation: Length scales, grid resolution, and accuracy," *Phys. Fluids*, **24** (1) , pp. 1–10 (2012) .

[19] Marconi, F. and Salas, M."Computation of Three Dimentional Flows about aircraft configurations," *Comput. Fluids*, **1** (2) , pp. 185–195 (1973) .

[20] Hashimoto, Atsushi, Furuta, Yasuyuki, Yagi, Naoto, and Nakamura, Yoshiaki"Analysis of a Fluttering Delta Wing with Large Deformation at Low Subsonic Speeds," *J. JAPAN Soc. Aeronaut. Sp. Sci.*, **55** (637) , pp. 104–110 (2007) .

[21] Hess, J. L. and Smith, A. M.O."Calculation of potential flow about arbitrary bodies," *Prog. Aerosp. Sci.*, **8** (C) , pp. 1–138 (1967) .

[22] Murman, Earll M. and Cole, Julian D."Calculation of plane steady transonic flows," *AIAA J.*, **9** (1) , pp. 114–121 (1971) .

[23] Kazemba, Cole D., Braun, Robert D., Clark, Ian G., and Schoenenberger, Mark"Survey of blunt-body supersonic dynamic stability," *J. Spacecr. Rockets*, **54** (1) , pp. 109–127 (2017) .

[24] Hiraki, Koju, Inatani, Yoshifumi, Ishii, Nobuaki, Nakajima, Takashi, and Hinada, Motoki"Dynamic Stability of MUSES-C Capsule," in *21st Int. Symp. Sp. Technol. Sci.*, pp. 945–950 (1998) .

[25] Hiraki, Koju"Experimental Study on Dynamic Instability of Capsule-shaped Body," *ISAS Rep.*, **103**, pp. 1–55 (1999) .

[26] Abe, Takashi, Sato, Syun-ichi, Matsukawa, Yutaka, Yamamoto, Kazuyuki, and Hiraoka, Katsumi"Study for dynamically unstable motion of reentry capsule," in *34th Thermophys. Conf.*, Reston, Virigina: American Institute of Aeronautics and Astronautics (2000) .

[27] Koga, Seigo, Hidaka, Akiko, Tagai, Rie, Kimura, Takeshi, Yoshinaga, Takashi, Nagai, Shinji, and Nishijima, Hironori"Dynamic Stability Testing of a Reentry Lifting Capsule in a Transonic Wind Tunnel," in *52nd Aerosp. Sci. Meet.* (January) , pp.

1–12, Reston, Virginia: American Institute of Aeronautics and Astronautics (2014) .

[28] Mitcheltree, Robert, Fremaux, Charles, and Yates, Leslie"Subsonic static and dynamic aerodynamics of blunt entry vehicles," in *37th Aerosp. Sci. Meet. Exhib.* (c) , Reston, Virigina: American Institute of Aeronautics and Astronautics (1999) .

[29] Ross, James and Brauckmann, Greg"Aerodynamic and Aeroacoustic Wind Tunnel Testing of the Orion Spacecraft," in *29th AIAA Appl. Aerodyn. Conf.*, Reston, Virigina: American Institute of Aeronautics and Astronautics (2011) .

[30] Mehta, R. C."Numerical simulation of supersonic flow past reentry capsules," *Shock Waves*, **15** (1) , pp. 31–41 (2006) .

[31] Nomura, Masayuki, Fujita, Koji, and Nagai, Hiroki"Computational Study of Aerodynamic Characteristics on Reentry Capsule Aft-body Shape in Transonic Flow," in *2018 AIAA Atmos. Flight Mech. Conf.* (209999) , Reston, Virginia: American Institute of Aeronautics and Astronautics (2018) .

[32] Ohmichi, Yuya, Kobayashi, Kenji, and Kanazaki, Masahiro"Numerical investigation of wake structures of an atmospheric entry capsule by modal analysis," *Phys. Fluids*, **31** (7) , p. 074105 (2019) .

[33] Teramoto, Susumu, Hiraki, Kouju, and Fujii, Kozo"Numerical analysis of dynamic stability of a reentry capsule at transonic speeds," *23rd Atmos. Flight Mech. Conf.*, **39** (4) , pp. 670–678 (1998) .

[34] Hashimoto, Atsushi, Murakami, Keiichi, Aoyama, Takashi, Tagai, Rie, Koga, Seigo, Nagai, Shinji, and Hayashi, Kenji"Dynamic Stability Analysis of a Reentry Lifting Capsule with Detached Eddy Simulation," in *54th AIAA Aerosp. Sci. Meet.* (January) , pp. 1–12, Reston, Virginia: American Institute of Aeronautics and Astronautics (2016) .

[35] Hirt, C. W., Amsden, A. A., and Cook, J. L."An Arbitrary Lagrangian-Eulerian

computing method for all flow speeds," *J. Comput. Phys.*, **135** (2) , pp. 203–216 (1997) .

[36] Steger, Joseph L."On application of body conforming curvilinear grids for finite difference solution of external flow," *Appl. Math. Comput.*, **10-11** (C) , pp. 295–316 (1982) .

[37] Aftosmis, M., Berger, M., and Adomavicius, G."A parallel multilevel method for adaptively refined Cartesian grids with embedded boundaries," in *38th Aerosp. Sci. Meet. Exhib.* (January) , Reston, Virigina: American Institute of Aeronautics and Astronautics (2000) .

[38] Miyoshi, Masaya, Mori, Koichi, and Nakamura, Yoshiaki"Numerical Simulation of Parachute Inflation Process by IB Method," *J. JAPAN Soc. Aeronaut. Sp. Sci.*, **57** (670) , pp. 419–425 (2009) , (in Japanese).

[39] Krajnović, Siniša, Ringqvist, Per, Nakade, Koji, and Basara, Branislav"Large eddy simulation of the flow around a simplified train moving through a crosswind flow," *J. Wind Eng. Ind. Aerodyn.*, **110**, pp. 86–99 (2012) .

[40] Schlichting, Hermann *Boundary-layer theory*: McGraw-Hill Book Company (1960)

[41] van Dyke, Milton *Perturbation methods in fluid mechanics*: The Parabolic Press (1975) .

[42] Shibata, M. *Asymptotic Series and Singular Perturbation Method*: Morikita Publishing, pp.83–111 (2009) , URL: `https://www.morikita.co.jp/books/book/442`, (in Japanese).

[43] Shima, Eiji and Kitamura, Keiichi"On New Simple Low-Dissipation Scheme of AUSM-Family for All Speeds," in *47th AIAA Aerosp. Sci. Meet. Incl. New Horizons Forum Aerosp. Expo.* (January) , pp. 1272–2010, Reston, Virigina: American Institute of Aeronautics and Astronautics (2009) .

[44] van Leer, Bram "Towards the ultimate conservative difference scheme. V. A second-order sequel to Godunov's method," *J. Comput. Phys.*, **32** (1) , pp. 101–136 (1979) .

[45] van Albada, G. D., van Leer, B., and Roberts, W. W. "A Comparative Study of Computational Methods in Cosmic Gas Dynamics," *Astron. Astrophys.*, **108**, pp. 76–84 (1982) .

[46] Thornber, B., Mosedale, A., Drikakis, D., Youngs, D., and Williams, R. J.R. "An improved reconstruction method for compressible flows with low Mach number features," *J. Comput. Phys.*, **227** (10) , pp. 4873–4894 (2008) .

[47] Shu, Chi-Wang and Osher, Stanley "Efficient implementation of essentially non-oscillatory shock-capturing schemes," *J. Comput. Phys.*, **77** (2) , pp. 439–471 (1988) .

[48] Abbott, Ira Herbert and Von Doenhoff, Albert Edward *Theory of Wing Sections, Including a Summary of Airfoil Data*: Dover Publications (1959) .

[49] Jameson, A. and Baker, T. "Solution of the Euler equations for complex configurations," in *6th Comput. Fluid Dyn. Conf. Danvers*, Reston, Virigina: American Institute of Aeronautics and Astronautics (1983) .

[50] Yagmur, Sercan, Dogan, Sercan, Aksoy, Muharrem Hilmi, Goktepeli, Ilker, and Ozgoren, Muammer "Comparison of flow characteristics around an equilateral triangular cylinder via PIV and Large Eddy Simulation methods," *Flow Meas. Instrum.*, **55** (February 2016) , pp. 23–36 (2017) .

[51] Lindsey, W. F. "Drag of Cylinders of Simple Shapes," *NACA Rep.*, **619** (1937) , URL: `https://ntrs.nasa.gov/search.jsp?R=19930091694`.

[52] Agrwal, Namit, Dutta, Sushanta, and Gandhi, B. K. "Experimental investigation of flow field behind triangular prisms at intermediate Reynolds number with different apex angles," *Exp. Therm. Fluid Sci.*, **72**, pp. 97–111 (2016) .

[53] LARSSON, Johan, KAWAI, Soshi, BODART, Julien, and BERMEJO-MORENO, Ivan"Large eddy simulation with modeled wall-stress: recent progress and future directions," *Mech. Eng. Rev.*, **3** (1) , pp. 15–00418–15–00418 (2016) .

[54] Fukushima, Yuma and Kawai, Soshi"Wall-modeled large-eddy simulation of transonic airfoil buffet at high reynolds number," *AIAA J.*, **56** (6) , pp. 2372–2388 (2018) .

[55] Lighthill, James *Fourier Analysis General Functions*: Cambridge University Press (1958) .

[56] Kim, Kyu Hong and Kim, Chongam"Accurate, efficient and monotonic numerical methods for multi-dimensional compressible flows," *J. Comput. Phys.*, **208** (2) , pp. 570–615 (2005) .

[57] Murayama, Mitsuhiro, Yokokawa, Yuzuru, Ura, Hiroki, Nakakita, Kazuyuki, Yamamoto, Kazuomi, Ito, Yasushi, Takaishi, Takehisa, Sakai, Ryotaro, Shimoda, Keiji, Kato, Takayuki, and Homma, Tomoyuki"Experimental Study of Slat Noise from 30P30N Three-Element High-Lift Airfoil in JAXA Kevlar-Wall Low-Speed Wind Tunnel," in *In Proceedings of the 2018 AIAA/CEAS Aeroacoustics Conference*, Reston, Virginia, USA: American Institute of Aeronautics and Astronautics (25–29 Jun 2018) .

[58] Pascioni, Kyle, Cattafesta, Louis N., and Choudhari, Meelan M."An Experimental Investigation of the 30P30N Multi-Element High-Lift Airfoil," in *In Proceedings of the 20th AIAA/CEAS Aeroacoustics Conference*, Reston, Virginia, USA: American Institute of Aeronautics and Astronautics (16–20 June 2014) .

[59] Sakai, Ryotaro, Ihida, Takashi, Murayama, Mitsuhiro, Ito, Yasushi, and Yamamoto, Kazuomi"Aerodynamic Simulation of 30P30N Airfoil using Second-Order Low-Dissipation Scheme on Cartesian Hybrid Grid," in *In Proceedings of Fifth Aerodynamics Prediction Challenge*, pp. 83–89, Tokyo, Japan: Japan Aerospace Exploration Agency (1 Jul 2019) .

[60] Ueno, Yosuke"Validation of Aerodynamic Noise from 3-Element High-Lift Airfoil Configulation using Cflow," in *In Proceedings of Fifth Aerodynamics Prediction Challenge*, pp. 103–116, Tokyo, Japan: Japan Aerospace Exploration Agency (1 Jul 2019) .

[61] Kazemba, Cole D., Braun, Robert D., Schoenenberger, Mark, and Clark, Ian G."Dynamic stability analysis of blunt-body entry vehicles using time-lagged aftbody pitching moments," *J. Spacecr. Rockets*, **52** (2) , pp. 393–403 (2015) .

[62] Hu, X. Y., Khoo, B. C., Adams, N. A., and Huang, F. L."A conservative interface method for compressible flows," *J. Comput. Phys.*, **219** (2) , pp. 553–578 (2006) .

[63] Martín, M. P., Taylor, E. M., Wu, M., and Weirs, V. G."A bandwidth-optimized WENO scheme for the effective direct numerical simulation of compressible turbulence," *J. Comput. Phys.*, **220** (1) , pp. 270–289 (2006) .

[64] Suzuki, Toshiyuki, Fujita, Kazuhisa, Yamada, Tetsuya, Inatani, Yoshifumi, and Ishii, Nobuaki"Postflight thermal protection system analysis of Hayabusa reentry capsule," *J. Spacecr. Rockets*, **51** (1) , pp. 96–105 (2014) .

Appendix A

Derivation of the Governing Equation using the Integral Form

A.1 Navier–Stokes Equation in the Integral Form

The governing equation is the compressible Navier–Stokes equation. Conservation laws over a cuboid control volume ($x_1 \leq x \leq x_2,\ y_1 \leq y \leq y_2,\ z_1 \leq z \leq z_2$) in the fluid can be written in the following integral form:

$$\begin{aligned}\frac{\mathrm{d}}{\mathrm{d}t}\int_{z_1}^{z_2}\int_{y_1}^{y_2}\int_{x_1}^{x_2}\boldsymbol{Q}\mathrm{d}x\mathrm{d}y\mathrm{d}z &+ \left[\int_{z_1}^{z_2}\int_{y_1}^{y_2}(\boldsymbol{E}_\mathrm{a}-\boldsymbol{E}_\mathrm{d})\mathrm{d}y\mathrm{d}z\right]_{x_1}^{x_2} \\ &+ \left[\int_{z_1}^{z_2}\int_{x_1}^{x_2}(\boldsymbol{F}_\mathrm{a}-\boldsymbol{F}_\mathrm{d})\mathrm{d}x\mathrm{d}z\right]_{y_1}^{y_2} \\ &+ \left[\int_{y_1}^{y_2}\int_{x_1}^{x_2}(\boldsymbol{G}_\mathrm{a}-\boldsymbol{G}_\mathrm{d})\mathrm{d}x\mathrm{d}y\right]_{z_1}^{z_2} = 0, \qquad \text{(A.1)}\end{aligned}$$

where $[f(x)]_{x_1}^{x_2}$ denotes $f(x_2) - f(x_1)$. The conserved quantities $\boldsymbol{Q}$; the advection fluxes $\boldsymbol{E}_\mathrm{a}$, $\boldsymbol{F}_\mathrm{a}$, and $\boldsymbol{G}_\mathrm{a}$; and the viscous and conductive fluxes $\boldsymbol{E}_\mathrm{d}$, $\boldsymbol{F}_\mathrm{d}$, and $\boldsymbol{G}_\mathrm{d}$ in Equation (A.1)

are defined as follows:

$$\boldsymbol{Q} = \begin{pmatrix} \rho \\ \rho u_x \\ \rho u_y \\ \rho u_z \\ e \end{pmatrix}, \quad \boldsymbol{E}_{\mathrm{a}} = \begin{pmatrix} \rho u_x \\ \rho u_x^2 + p \\ \rho u_y u_x \\ \rho u_z u_x \\ e u_x + p u_x \end{pmatrix}, \quad \boldsymbol{F}_{\mathrm{a}} = \begin{pmatrix} \rho u_y \\ \rho u_x u_y \\ \rho u_y^2 + p \\ \rho u_z u_y \\ e u_y + p u_y \end{pmatrix}, \quad \boldsymbol{G}_{\mathrm{a}} = \begin{pmatrix} \rho u_z \\ \rho u_x u_z \\ \rho u_y u_z \\ \rho u_z^2 + p \\ e u_z + p u_z \end{pmatrix},$$

$$\boldsymbol{E}_{\mathrm{d}} = \begin{pmatrix} 0 \\ \tau_{xx} \\ \tau_{yx} \\ \tau_{zx} \\ u_x \tau_{xx} + u_y \tau_{yx} + u_z \tau_{zx} - q_x \end{pmatrix}, \quad \boldsymbol{F}_{\mathrm{d}} = \begin{pmatrix} 0 \\ \tau_{xy} \\ \tau_{yy} \\ \tau_{zy} \\ u_x \tau_{xy} + u_y \tau_{yy} + u_z \tau_{zy} - q_y \end{pmatrix},$$

$$\boldsymbol{G}_{\mathrm{d}} = \begin{pmatrix} 0 \\ \tau_{xz} \\ \tau_{yz} \\ \tau_{zz} \\ u_x \tau_{zx} + u_y \tau_{yz} + u_z \tau_{zz} - q_z \end{pmatrix}, \tag{A.2}$$

where ρ is the density; u_x, u_y, and u_z are the components of the velocity; p is the pressure; and e is the total energy per unit volume. The variables $\boldsymbol{\tau}$ and $\boldsymbol{q}$ are the stress tensor and heat flux, respectively:

$$\begin{aligned}
\tau_{xx} &= \frac{2}{3}\mu\left(2\frac{\partial u_x}{\partial x} - \frac{\partial u_y}{\partial y} - \frac{\partial u_z}{\partial z}\right), \\
\tau_{yy} &= \frac{2}{3}\mu\left(2\frac{\partial u_y}{\partial y} - \frac{\partial u_z}{\partial z} - \frac{\partial u_x}{\partial x}\right), \\
\tau_{zz} &= \frac{2}{3}\mu\left(2\frac{\partial u_z}{\partial z} - \frac{\partial u_x}{\partial x} - \frac{\partial u_y}{\partial y}\right), \\
\tau_{xy} &= \tau_{yx} = \mu\left(\frac{\partial u_x}{\partial y} + \frac{\partial u_y}{\partial x}\right), \\
\tau_{yz} &= \tau_{zy} = \mu\left(\frac{\partial u_y}{\partial z} + \frac{\partial u_z}{\partial y}\right), \\
\tau_{zx} &= \tau_{xz} = \mu\left(\frac{\partial u_z}{\partial x} + \frac{\partial u_x}{\partial z}\right).
\end{aligned} \tag{A.3}$$

$$\begin{aligned}
q_x &= -\frac{1}{\gamma - 1}\frac{\mu}{Pr}\frac{\partial a^2}{\partial x}, \\
q_y &= -\frac{1}{\gamma - 1}\frac{\mu}{Pr}\frac{\partial a^2}{\partial y}, \\
q_z &= -\frac{1}{\gamma - 1}\frac{\mu}{Pr}\frac{\partial a^2}{\partial z},
\end{aligned} \tag{A.4}$$

where a is the speed of sound; μ is the viscosity obtained by Sutherland's law; and the Prandtl number Pr is 0.72.

A.2 Extension of the Navier–Stokes Equation to the Cartesian Cut-Cell Method

The conservation equation in integral form over a cuboid control volume that extends over the two regions of the air and the object is written in the following form using the Heaviside function $H(x, y, z)$:

$$\begin{aligned}\frac{\mathrm{d}}{\mathrm{d}t}\int_{z_1}^{z_2}\int_{y_1}^{y_2}\int_{x_1}^{x_2} H\boldsymbol{Q}\mathrm{d}x\mathrm{d}y\mathrm{d}z &+ \left[\int_{z_1}^{z_2}\int_{y_1}^{y_2} H(\boldsymbol{E}_\mathrm{a}-\boldsymbol{E}_\mathrm{d})\mathrm{d}y\mathrm{d}z\right]_{x_1}^{x_2} \\ &+ \left[\int_{z_1}^{z_2}\int_{x_1}^{x_2} H(\boldsymbol{F}_\mathrm{a}-\boldsymbol{F}_\mathrm{d})\mathrm{d}x\mathrm{d}z\right]_{y_1}^{y_2} \\ &+ \left[\int_{y_1}^{y_2}\int_{x_1}^{x_2} H(\boldsymbol{G}_\mathrm{a}-\boldsymbol{G}_\mathrm{d})\mathrm{d}x\mathrm{d}y\right]_{z_1}^{z_2} \\ &- \iint_{\text{cut-plane}} \{(\boldsymbol{E}_\mathrm{a}-\boldsymbol{E}_\mathrm{d})n_x + (\boldsymbol{F}_\mathrm{a}-\boldsymbol{F}_\mathrm{d})n_y + (\boldsymbol{G}_\mathrm{a}-\boldsymbol{G}_\mathrm{d})n_z\}\,\mathrm{d}S = 0,\end{aligned} \tag{A.5}$$

where the Heaviside function $H(x, y, z)$ gives $H = 1$ in the air and $H = 0$ in the object; and the vector $\boldsymbol{n}$ represents the unit normal vector directed outward form the object into the air. Considering the boundary condition $\boldsymbol{u}\cdot\boldsymbol{n} = 0$ at the object surface, Equation (A.5) is reduced to the following form:

$$\begin{aligned}\frac{\mathrm{d}}{\mathrm{d}t}\int_{z_1}^{z_2}\int_{y_1}^{y_2}\int_{x_1}^{x_2} H\boldsymbol{Q}\mathrm{d}x\mathrm{d}y\mathrm{d}z &+ \left[\int_{z_1}^{z_2}\int_{y_1}^{y_2} H(\boldsymbol{E}_\mathrm{a}-\boldsymbol{E}_\mathrm{d})\mathrm{d}y\mathrm{d}z\right]_{x_1}^{x_2} \\ &+ \left[\int_{z_1}^{z_2}\int_{x_1}^{x_2} H(\boldsymbol{F}_\mathrm{a}-\boldsymbol{F}_\mathrm{d})\mathrm{d}x\mathrm{d}z\right]_{y_1}^{y_2} \\ &+ \left[\int_{y_1}^{y_2}\int_{x_1}^{x_2} H(\boldsymbol{G}_\mathrm{a}-\boldsymbol{G}_\mathrm{d})\mathrm{d}x\mathrm{d}y\right]_{z_1}^{z_2} = \iint_{\text{cut-plane}} \boldsymbol{\sigma}\mathrm{d}S,\end{aligned} \tag{A.6}$$

where the variable $\boldsymbol{\sigma}$ on the right-hand side of Equation (A.6) represents the wall flux vector (the interaction between the object and the air), which is directed from the object into the air:

$$\boldsymbol{\sigma} = \begin{pmatrix} 0 \\ pn_x - \tau_{xx}n_x - \tau_{xy}n_y - \tau_{xz}n_z \\ pn_y - \tau_{yx}n_x - \tau_{yy}n_y - \tau_{yz}n_z \\ pn_z - \tau_{zx}n_x - \tau_{zy}n_y - \tau_{zz}n_z \\ 0 \end{pmatrix} \simeq \begin{pmatrix} 0 \\ pn_x - \tau_w b_x \\ pn_y - \tau_w b_y \\ pn_z - \tau_w b_z \\ 0 \end{pmatrix}. \tag{A.7}$$

The vector $\boldsymbol{b}$ is the stream-wise unit vector parallel to the wall. The scalar value τ_w of the wall shear stress is obtained by the wall-stress model. Wall flux of mentum through

the pressure and the shear stress are included, while wall flux of mass and energy do not exist in the problems considered here.

The governing equation (A.6) is solved using a cell-centered finite volume method. Cell-averaged quantities of the finite volume method are defined as follows:

$$
\begin{aligned}
&\bar{\boldsymbol{Q}} = \frac{1}{\alpha V}\int_{z_1}^{z_2}\int_{y_1}^{y_2}\int_{x_1}^{x_2} H\boldsymbol{Q}\mathrm{d}x\mathrm{d}y\mathrm{d}z, && \alpha = \frac{1}{V}\int_{z_1}^{z_2}\int_{y_1}^{y_2}\int_{x_1}^{x_2} H\mathrm{d}x\mathrm{d}y\mathrm{d}z,\\
&V = (x_2-x_1)(y_2-y_1)(z_2-z_1),\\
&\bar{\boldsymbol{E}}_\mathrm{a} - \bar{\boldsymbol{E}}_\mathrm{d} = \frac{1}{\beta_x S_x}\int_{z_1}^{z_2}\int_{y_1}^{y_2} H(\boldsymbol{E}_\mathrm{a}-\boldsymbol{E}_\mathrm{d})\mathrm{d}y\mathrm{d}z, && \beta_x = \frac{1}{S_x}\int_{z_1}^{z_2}\int_{y_1}^{y_2} H\mathrm{d}y\mathrm{d}z,\\
&S_x = (y_2-y_1)(z_2-z_1),\\
&\bar{\boldsymbol{F}}_\mathrm{a} - \bar{\boldsymbol{F}}_\mathrm{d} = \frac{1}{\beta_y S_y}\int_{z_1}^{z_2}\int_{x_1}^{x_2} H(\boldsymbol{F}_\mathrm{a}-\boldsymbol{F}_\mathrm{d})\mathrm{d}x\mathrm{d}z, && \beta_y = \frac{1}{S_y}\int_{z_1}^{z_2}\int_{x_1}^{x_2} H\mathrm{d}x\mathrm{d}z,\\
&S_y = (x_2-x_1)(z_2-z_1),\\
&\bar{\boldsymbol{G}}_\mathrm{a} - \bar{\boldsymbol{G}}_\mathrm{d} = \frac{1}{\beta_z S_z}\int_{y_1}^{y_2}\int_{x_1}^{x_2} H(\boldsymbol{G}_\mathrm{a}-\boldsymbol{G}_\mathrm{d})\mathrm{d}x\mathrm{d}y, && \beta_z = \frac{1}{S_z}\int_{y_1}^{y_2}\int_{x_1}^{x_2} H\mathrm{d}x\mathrm{d}y,\\
&S_z = (x_2-x_1)(y_2-y_1),\\
&\bar{\boldsymbol{\sigma}} = \frac{1}{S_{\text{cut-plane}}} = \iint_{\text{cut-plane}} \boldsymbol{\sigma}\mathrm{d}S, && S_{\text{cut-plane}} = \iint_{\text{cut-plane}} \mathrm{d}S, \qquad \text{(A.8)}
\end{aligned}
$$

where α is the volume fraction of the air in the cell; β_x, β_y, β_z are the area fractions of the air in each cell interface; V is the volume of the cell; and S_x, S_y, and S_z are the area of each cell interfaces. Using these cell-averaged values, governing equation (A.6) is reduced to the following form:

$$
\frac{\mathrm{d}\alpha\bar{\boldsymbol{Q}}}{\mathrm{d}t} + \frac{\left[\beta_x(\bar{\boldsymbol{E}}_\mathrm{a}-\bar{\boldsymbol{E}}_\mathrm{d})\right]_{x_1}^{x_2}}{x_2-x_1} + \frac{\left[\beta_y(\bar{\boldsymbol{F}}_\mathrm{a}-\bar{\boldsymbol{F}}_\mathrm{d})\right]_{y_1}^{y_2}}{y_2-y_1} + \frac{\left[\beta_z(\bar{\boldsymbol{G}}_\mathrm{a}-\bar{\boldsymbol{G}}_\mathrm{d})\right]_{z_1}^{z_2}}{z_2-z_1} = \frac{S_{\text{cut-plane}}}{V}\bar{\boldsymbol{\sigma}}. \qquad \text{(A.9)}
$$

The projection of the cut plane to each cell interface is approximated in the following form:

$$
S_{\text{cut-plane}}n_x \simeq [\beta_x]_{x_1}^{x_2} S_x, \qquad S_{\text{cut-plane}}n_y \simeq [\beta_y]_{y_1}^{y_2} S_y, \qquad S_{\text{cut-plane}}n_z \simeq [\beta_z]_{z_1}^{z_2} S_z. \qquad \text{(A.10)}
$$

These approximation tend to be exact equations at the limit of small curvature of the cut plane. Thus in the case of the sufficiently small control volume, $S_{\text{cut-plane}}$ and $\boldsymbol{n}$ are evaluated as follows:

$$
S_{\text{cut-plane}} = \left\{ \left([\beta_x]_{x_1}^{x_2} S_x\right)^2 + \left([\beta_y]_{y_1}^{y_2} S_y\right)^2 + \left([\beta_z]_{z_1}^{z_2} S_z\right)^2 \right\}^{1/2}, \qquad \text{(A.11)}
$$

$$
n_x = \frac{V\,[\beta_x]_{x_1}^{x_2}}{S_{\text{cut-plane}}(x_2-x_1)}, \quad n_y = \frac{V\,[\beta_y]_{y_1}^{y_2}}{S_{\text{cut-plane}}(y_2-y_1)}, \quad n_z = \frac{V\,[\beta_z]_{z_1}^{z_2}}{S_{\text{cut-plane}}(z_2-z_1)}. \qquad \text{(A.12)}
$$

Acknowledgments

I am grateful to Prof. Kazuyuki Ueno for helpful discussions and guidance since my bachelor's course. I could make a decision to admission to the doctor course, thanks to the recommendation by Prof. Ueno. My foundation of the researcher is made by the six years in the Ueno lab.

I have greatly benefited from Drs. Hideyuki Tanno and Shingo Matsuyama for helpful discussions for writing a journal paper which is used as a chapter in my doctoral thesis.

I sincerely appreciate the discussion with Profs. Ken-ichi Funazaki and Hideki Yanaoka, the examination committee of this doctoral thesis.

I gratefully acknowledge contributions and discussions with the past and present members of our laboratory especially the member of the compressible CFD group in Ueno Lab., Mr. Makito Nakamura, Mr. Tatsuya Ishikawa, Mr. Tomohiro Okudera, Ms. Kasumi Omizu, and Mr. Yuta Takahashi.

I am deeply grateful to my parents and grandparents for the kindness and support for my graduation.

The end of the acknowledgement, I want to thank my best friend Shota Kusanagi.

Part of the experimental results in this research were obtained using supercomputing resources at the Cyberscience Center, Tohoku University.